

Arunn Kamalaraja

Investigation of corner vortex in radial cascade and interaction with the trailing edge vortex

Master's thesis in Mechanical Engineering
June 2021

Arunn Kamalaraja

Investigation of corner vortex in radial cascade and interaction with the trailing edge vortex

Master's thesis in Mechanical Engineering
Supervisor: Chirag Trivedi
Co-supervisor: Pål-Tore Selbo Storli
June 2021

Norwegian University of Science and Technology
Faculty of Engineering
Department of Energy and Process Engineering



Master`s Agreement / Main Thesis Agreement

Faculty	Faculty of Engineering
Institute	Department of Energy and Process Engineering
Programme Code	MTPROD
Course Code	TEP4925

Personal Information	
Surname, First Name	Kamalaraja, Arunn
Date of Birth	06.06.1996
Email	arunnk@stud.ntnu.no

Supervision and Co-authors	
Supervisor	Chirag Trivedi
Co-supervisors (if applicable)	Pål-Tore Selbo Storli
Co-authors (if applicable)	

The Master`s thesis	
Starting Date	11.01.2021
Submission Deadline	11.06.2021
Thesis Working Title	Investigation of corner vortex in radial cascade and interaction with the trailing edge vortex
Problem Description	<p>Turbine blades have different characteristic frequencies, where the role of trailing edge is crucial. Frequencies and amplitudes of vortex shedding are dependent on the trailing edge profiles. Trailing edge vortex have been studies from decades however, when the trailing edge vortex interacts with the corner vortex (also known as hub vortex in hydraulic turbines), flow mechanics is quite different. The present work is continuation of project work conducted during Autumn 2020. The project work aimed to study fluid mechanics of flow through simplified radial cascade. The study was carried out using computational fluid dynamic technique. The student focused on one trailing edge profile and carried out preliminary study on the inception of corner vortex. A radial cascade of three blades was developed and studied numerically. 1. The following tasks are to be considered During the master thesis work, the student will focus on interaction of trailing edge vortex and the corner vortex considering the fluid mechanic aspect. The student will aim to</p>

	<p>investigate the characteristics of vortex interaction using high quality numerical modelling approach. Following tasks are expected to carry out for the master thesis work. □ Preparing a robust numerical model of the circular cascade, focus should be hexahedral mesh high quality discretization of the domain and more accurate boundary layers. □ Resolve turbulent structure, specifically at the trailing edge. □ Consider at-least three trailing edge profile, three different flow conditions, three asymmetric hydrofoil profiles, three values of angle of attack. This defines the range of simulation with 81 parameters. Considering the CPU limitations, at-least 9 different parameters should be investigated. □ These parameters will provide comprehensive view on the formation of trailing edge vortex, turbulent structure, length scales, turbulent intensity, vorticity, and velocity magnitude. □ The selection of hydrofoil profiles should be identical to the hydro turbine blades. □ It is also recommended to consider angular rotation of the hydrofoil, i.e., axial flow runner.</p>
--	---



Abstract

Vortex shedding is a fluid phenomenon encountered in a wide variety of engineering applications. The phenomenon is capable of inducing severe vibration whenever the frequency of the vortex shedding overlap with one of the structure's natural frequencies. In the context of hydraulic turbines, it's an important flow feature to mitigate. However, mechanical challenges are appearing in the new age of hydropower. Where the turbine blades are manufactured thinner to increase the hydraulic efficiency. At the same, hydropower plants are increasingly required to operate beyond their designed range. This has resulted in a higher dynamic load on the turbine structure. Consequently, several structural failures have been reported in the last decade, making it a growing concern. Thus, it is important to properly understand such a phenomenon.

Turbine blades have different vortex shedding characteristic that depends on the trailing edge shape. However, when the trailing edge vortex interacts with the corner vortex, which is also known as the hub vortex, in hydraulic turbines, the wake characteristic changes. The present work investigates vortex shedding and its interaction with the corner vortex. A three-dimensional radial cascade of three blades is prepared and simulated for different trailing edge profiles. Simulations were performed for NACA6412 hydrofoils with truncated, symmetric, and oblique trailing edges at three angles of attack each. A shear stress transport-scale adaptive simulation (SST-SAS) model was employed with a chord-based Reynolds number of $3.0 \cdot 10^5$.

Vortex shedding frequency was determined for each hydrofoil. The results show that the oblique trailing edge yields the maximum shedding frequency. The study indicates that an increase in the angle of attack led to an increase of vortex shedding frequency. On the other hand, vortex strength is inversely proportional to the corresponding shedding frequency.

Interaction of corner vortex was analysed with a qualitative approach. The results showed that the corner vortex develop differently depending on the trailing edge shape. The truncated trailing edge shape illustrated a more turbulent corner vortex downstream compared to other hydrofoils. The corner vortex is indicated to influence the configuration of vortex shedding along the span. However, the interaction is not well understood. When the angle of attack increased, vortex shedding was parallel and stronger near the hub, which suggests that the frequency can be altered along the span by the corner vortex generated in hydraulic turbines. This requires further research.



Sammendrag

Virvelavløsning fra objekter er et strømningsfenomen som kan finnes blant industrielle applikasjoner. Strømningsfenomenet avløser virvler som fører til vibrasjon. Denne vibrasjonen kan forsterkes, dersom virvelavløsningsfrekvensen sammenfaller med egenfrekvensen til et objekt. I sammenheng med vannkraft, er det spesielt viktig å unngå vibrasjon. I de siste tiårene med vannkraft har jakten på økt hydraulisk effektivitet og kostnadseffektive blader ført til produksjon av tynnere blader i hydrauliske turbiner. Samtidig opererer vannkraftverk stadig mer utenfor sitt optimale lastområde. Dette har ført til høyere dynamiske belastninger på bladene, noe som gjør dem mer utsatt for utmattelsessprengning. Følgelig har det skjedd flere strukturelle feil det siste tiåret, noe som gjør det til en økende bekymring. Derfor, er det viktig å forstå strømningsfenomenet.

Turbin blader har forskjellige karakteristikk for virvelavløsning, avhengig av formen til bakkanten. Men når virvelavløsningsfenomenet reagerer med andre sekundære virvelfenomener som utvikles langs rot veggen, kan strømningskarakteristikken nedstrøm for bakkanten bli endret. Denne oppgaven undersøker interaksjonen mellom virvelavløsning og hjørnevirvel. En tredimensjonal sirkulær kaskade av tre blader har blitt utviklet. Simulering i form av numerisk strømningsberegning har blitt utført for ulike bakkant geometrier. Simuleringene har blitt utført for NACA 6412 hydrofoiler med avstumpet, asymmetrisk, og symmetrisk bakkant. I tillegg har hydrofoilene blitt simulert for tre ulike angrepsvinkler. Turbulensmodellen shear stress transport-scale adaptive simulation (SST-SAS) har blitt brukt til å simulere. Det korde-basert Reynoldstallet er omtrent $3.0 \cdot 10^5$.

Virvelavløsningsfrekvensen ble bestemt for hver hydrofoil. Resultatene viser at hydrofoilen med asymmetrisk bakkant gir høyest virvelavløsningsfrekvens. Videre, fører økning av angrepsvinkel til høyere virvelavløsningsfrekvens. Resultatene tyder på at virvel styrken er omvendt proporsjonal med virvelavløsningsfrekvensen.

Interaksjonen med hjørnevirkelen ble analysert med kvalitativ tilnærming. Resultatene viser at hjørnevirkelen utvikler seg forskjellig avhengig av formen på bakkanten. Bakkanten med avstump utviklet en noe mer turbulent hjørnevirkel sammenlignet med de andre bakkantene. Virvelavløsningsfenomenet langs spennvidde på hydrofoilen, indikerer å være påvirket av hjørnevirkelen. Men dette samspillet er ikke forstått. Når angrepsvinkelen øker, blir virvelavløsningsfenomenet sterkere og parallell i nærheten av indre turbin vegg. Dette antyder at virvelfrekvensen langs spennvidden kan bli forandret av hjørnevirkler som dannes i hydrauliske turbiner. Noe som krever videre forskning.

Acknowledgments

This work has been conducted at the [Waterpower Laboratory](#), Department of Energy and Process Engineering at the Norwegian University of Science and Technology (NTNU) in Trondheim.

Numerical simulations presented in the thesis are conducted under using [IDUN](#) computing cluster. The cluster has more than 70 nodes and 90 GPGPUs. Each node contains two Intel Xeon cores, at least 128 GB of main memory, and is connected to an Infiniband network. Half of the nodes are equipped with two or more Nvidia Tesla P100 or V100 GPGPUs. Idun's storage is provided by two storage arrays and a Lustre parallel distributed file system

I would like to express my deepest gratitude to my supervisor, associate professor Chirag Trivedi at the Waterpower Laboratory at NTNU for providing support and guidance during my work with the master thesis. His knowledge and experience regarding computational fluid dynamics (CFD) were extremely valuable for my work. Chirag Trivedi has always gone the extra mile to help whenever new challenges and problems arose.

Lastly, I would like to acknowledge the people at the Waterpower Laboratory for making this year great.

Contents

Abstract	i
Sammendrag	iii
Acknowledgments	v
Contents	vii
List of tables	ix
List of figures	xii
Nomenclature	xiii
1 Introduction	1
1.1 Background	1
1.2 The objective	3
2 Literature review	5
3 Theory	9

3.1	Vorticity	9
3.2	Secondary flow	12
3.3	Frequency of vortex shedding	14
3.4	Turbulence	17
3.5	Computational fluid dynamics	18
3.6	Turbulence models	20
4	Numerical method	25
4.1	Model description	25
4.2	Meshing approach	27
4.3	Numerical setup	29
4.4	Solution verification	32
5	Results and discussions	35
5.1	Vortex shedding frequency	35
5.2	Interaction of hub vortex	42
6	Conclusions	49
7	Future work	51
	References	53
A	Appendix A	57
A.1	Geometry coordinates	57

List of Tables

4.1	Selected boundary condition and other parameters for the simulation.	32
4.2	Discretization error estimation.	34
5.1	vortex shedding frequency at $\alpha = 0^\circ, 3^\circ$, and 6°	40

List of Figures

1.1	Vortex shedding around a cylinder [1]	2
2.1	Trailing edges used in the work of Heskestad and Olberts [2]. . .	5
2.2	Vortex shedding frequency versus reference velocity, C_{ref} . Experimental result for a truncated and oblique trailing edge. Lock-in is occur around 10-15 m/s [3].	6
3.1	Rotation of fluid element in a mono-directional shear flow [4]. . .	10
3.2	Generation of streamwise vorticity component (secondary flow) from convection of vortex lines [4].	12
3.3	Boundary layer vortex lines wrapping around leading edge [4]. . .	13
3.4	Secondary flow model by Wang et al.(1997).	14
3.5	Relationship between Strouhal number and Reynolds number for circular cylinders [5].	15
3.6	Trailing edge of hydrofoil with relative amplitude A and value of geometrical constant B [6].	17
3.7	Cylinder in cross flow at Reynolds number of $3 \cdot 10^6$. Left: URANS. Right: SAS [7].	23
4.1	NACA 6412.	25
4.2	Trailing edge geometry.	26

4.3	Radial cascade geometry.	27
4.4	Numerical model of radial cascade.	28
4.5	Numerical grid of blade passage.	29
4.6	Mesh topology around trailing edge.	30
4.7	Mesh distribution along hydrofoil span.	31
4.8	Model with boundary conditions.	33
5.1	Instantaneous vorticity field at 50% span for $\alpha = 0^\circ$	36
5.2	Amplitude frequency spectrum for hydrofoil trailing edges at $\alpha = 0^\circ$	37
5.3	Instantaneous vorticity field at 50% span at $\alpha = 3^\circ$	38
5.4	Amplitude frequency spectrum for hydrofoils at $\alpha = 3^\circ$	39
5.5	Instantaneous vorticity field at 50% span at $\alpha = 6^\circ$	40
5.6	Amplitude frequency spectrum for hydrofoils at $\alpha = 6^\circ$	41
5.7	The cross flow velocity component is depicted for hydrofoils at $\alpha = 0^\circ$	43
5.8	Streamwise vorticity is shown on planes perpendicular to mean flow for hydrofoils at $\alpha = 0^\circ$	43
5.9	The cross flow velocity component is depicted for hydrofoils at $\alpha = 3^\circ$	44
5.10	Streamwise vorticity is shown on planes perpendicular to mean flow for hydrofoils at $\alpha = 3^\circ$	45
5.11	The cross flow velocity component is depicted for hydrofoils at $\alpha = 6^\circ$	46
5.12	Streamwise vorticity is shown on planes perpendicular to mean flow for hydrofoils at $\alpha = 6^\circ$	47
5.13	Streamwise velocity field on blade surface with 0.5 mm surface offset. $\alpha = 6^\circ$	48

Nomenclature

Abbreviation

CFD	Computational fluid dynamics
DNS	Direct numerical simulation
FFT	Fast fourier transform
LES	Large eddy simulation
NTNU	Norwegian University of Science and Technology
RMS	Root mean square
RANS	Reynolds-average Navier-stokes
SAS	Scale adaptive simulation
SST	Shear stress transport
URANS	Unsteady Reynolds-average Navier-stokes

Latin symbols

D	Characteristic length (m)
f_s	Shedding frequency (Hz)
k	Turbulent kinetic energy ($\text{m}^2 \text{s}^{-2}$)
L	Characteristic length (m)
P	Mean pressure (Pa)

p	Instantaneous pressure (Pa)
S_{ij}	Mean strain rate(s^{-1})
t	Blade thickness at trailing edge (mm)
T	Time averaging interval (s)
Δt	Time step (s)
U	Mean x-component of velocity ($m s^{-1}$)
U_{∞}	Free stream velocity ($m s^{-1}$)
\mathbf{U}	Mean velocity vector ($m s^{-1}$)
U	Mean x-component of velocity ($m s^{-1}$)
u	Instantaneous x-component of velocity ($m s^{-1}$)
V	Mean y-component of velocity ($m s^{-1}$)
v	instantaneous y-component of velocity ($m s^{-1}$)
W	Mean z-component of velocity ($m s^{-1}$)
w	Instantaneous z-component of velocity ($m s^{-1}$)

Dimensionless numbers

e_a	Approximate relative error
e_{ext}	Extrapolated relative error
GCI	Grid convergence index
I	Turbulence intensity
Re	Reynolds number
St	Strouhal number

Greek symbols

μ	Dynamic viscosity ($kg m^{-1} s^{-1}$)
ρ	Density ($kg m^{-3}$)
ϵ	Dissipation rate of turbulent kinetic energy ($m^2 s^{-3}$)

δ_{ij}	Kronecker delta
ν	Kinematic viscosity ($\text{m}^2 \text{s}^{-1}$)
ϕ	Scalar variable
ϕ'	Fluctuation of scalar variable
μ_t	Turbulent/eddy viscosity ($\text{kg m}^{-1} \text{s}^{-1}$)
ω	Turbulence frequency (Hz)

Superscripts and subscripts

$\overline{(\)}$	average of variable
$(\)'$	Fluctuation of variable
$(\)_{ij}$	Newton suffix

Chapter 1

Introduction

1.1 Background

In the last century, climate change has become a topic of great interest. Its devastating effect around the world is raising awareness regarding greenhouse gases. With the 2016 Paris agreement, there is an increased pressure to reduce fossil fuel-based energy sources. Today, almost 80% of the global energy mix is produced from fossil fuel [8]. It is only a matter of time before this ratio will considerably change, as renewable energy sources such as solar and wind power are in an increasing number being installed and employed.

The introduction of intermittent power production from renewable sources such as solar and wind poses a demand in the market for flexibility to maintain stable and available clean energy to a growing world population [9]. Therefore, it is important with an energy system that can store energy and provide whenever the intermittent energy source can not cover the power demand. Hydropower is a well developed source of energy that enables power to quickly be produced and is capable of storing water in reservoirs for later power production. Therefore, hydropower benefits the power grid, as it offers flexibility to the power grid.

As hydropower is taking on the role of a flexible power source, hydraulic turbines are required to operate over a wider range [10]. Thus they are pushed to operate beyond their designated point of optimal efficiency. This means that structural components within hydraulic turbines are exposed to higher dynamic loads [11]. At the same time, turbine blades are designed thinner to reduced material cost and increase hydraulic efficiency, which has left them more susceptible to higher cyclic stress. Consequently, several turbine runners have failed due to fatigue cracking in the last decade [12]. This motivates for a better understanding of fluid flow in hydraulics turbines.



Figure 1.1: Vortex shedding around a cylinder [1]

There exist several undesirable fluid phenomena that induce structural vibration on turbine blades. One of such is the von Kármán vortex shedding at the trailing edge of a blade. This flow phenomenon is encountered in many engineering application and is a characteristic flow feature in the wake of bluff bodies. Figure 1.1 illustrate a von Kármán vortex street in the wake of a circular cylinder. Griffin [13] and Williamson et al. [14] explained that this process is caused by the separation of shear layer on the upper and lower surfaces. The velocity gradient in the shear layers causes them to roll up into a pair of vortices. At some point, one of the two vortices will grow in strength until its sufficiently strong to pull the adjacent vortex across the wake. The adjacent vortex which has the opposite circulation will then cut the first vortex free. The first vortex is then shed downstream of the trailing edge. This process will repeat itself, thereby shedding vortices in an oscillating manner. As this occurs, the local pressure correspondingly oscillates and induce mechanical vibration. The vibration caused by vortex shedding is particularly amplified if the vortex shedding frequency approaches a natural frequency of the blade.

Turbine blades have different shedding characteristic, where the role of trailing edge is crucial. It is well known that frequency and amplitude are highly influenced by the trailing edge property. However, when the trailing edge vortex interacts with the corner vortex, which is also known as hub vortex in hydraulic turbines, the flow characteristic changes. However, the complex nature of flow field in hydraulic turbines makes it extremely challenging to study this phenomenon without isolating others. Thus, isolated simplified study is important, allowing us to study one phenomenon in detail. In light of this, computational fluid dynamics (CFD) analysis of a simplified radial cascade was performed to investigate vortex interaction in a variety of operating condition.

1.2 The objective

The objective of this master thesis was to perform CFD simulation of a simplified radial cascade to investigate the trailing edge vortex and its interaction with the corner vortex. In order to elucidate the dynamic of vortex interaction numerical simulation have been performed for NACA 6412 hydrofoils with three angles of attack for each design of the trailing edge. Total three trailing edges were selected for the investigation.

The present work is a continuation of the project work [15]. The following sections are partly reused and modified: 3.6, 3.7 and 3.7. Chapter 4 will also bear some resemblance since the same methodology is employed in the project work.

Chapter 2

Literature review

Vortex shedding is a flow phenomenon encountered in many engineering applications, and is a characteristic flow feature in the wake of bluff bodies. The vortex shedding phenomenon has been extensively studied since it was observed behind cylinders by Vincent Strohaul in 1878 [16]. Through various studies, it was reported that intense vibration can occur if the vortex shedding frequency coincides with the eigenfrequency of a body [17]. This finding shifted attention of the study of vortex shedding from cylindrical object to object with practical interest, like hydrofoils. Despite its relevance to engineering problems in hydraulic turbines, pumps and marine propellers, hydrofoils have been investigated to a much lesser extent in comparison with cylinders and squares, which has served as a benchmark problem for the von Kármán vortex shedding.

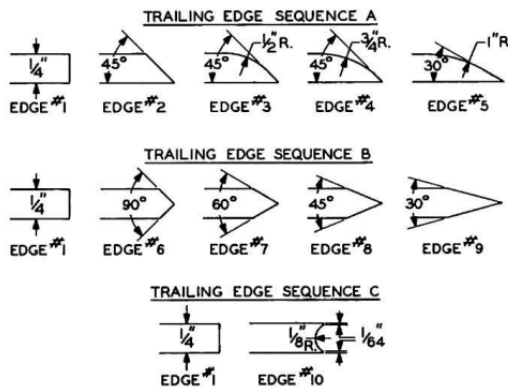


Figure 2.1: Trailing edges used in the work of Heskestad and Olberts [2].

In the paper by Heskestad and Olberts [2], the influence of trailing edge geometry

on hydraulic turbine blade vibration resulting from vortex excitation was investigated. In this study, Heskestad and Olberts systematically study different trailing edges, with a detailed study on the variation of angles for different trailing edges, as depicted in Figure 2.1. The study shows that the frequency of vortex shedding is highly dependent on the trailing edge geometry. In the symmetric trailing edges they observed that a more protruded trailing edge yielded an increase in vortex strength and reduction in frequency due to the "shielding" effect between the regions of vortex growth provided by the symmetric extension. Going through the asymmetric trailing edges, the separation points approach each other, which increase the degree of vortex velocity field overlap. This results in a reduction of the generated vortex strength, but an increase in frequency. From their study, they concluded that vortex strength is primarily a function of the distance between the separation points, degree of shielding and the frequency of the vortex shedding. Their result also indicated that vortex strength and shedding frequency are inversely proportional to each other.

Ausoni et al. [18] experimentally investigated the von Kármán vortex shedding in the wake of a 2D symmetrical hydrofoil with a truncated trailing edge. They analysed the fluid-structure interaction at a zero degree angle of attack, with Reynolds number ranging from $5.0 \cdot 10^5 \leq Re \leq 2.0 \cdot 10^6$. Their results showed the shedding frequency to increase linearly with velocity, except in the region around resonance frequency, where a lock-in phenomenon occurs. Under lock-off, i.e. no resonance frequency is excited, the von Kármán vortices exhibit spanwise 3D instabilities, seen as curved vorticity lines.

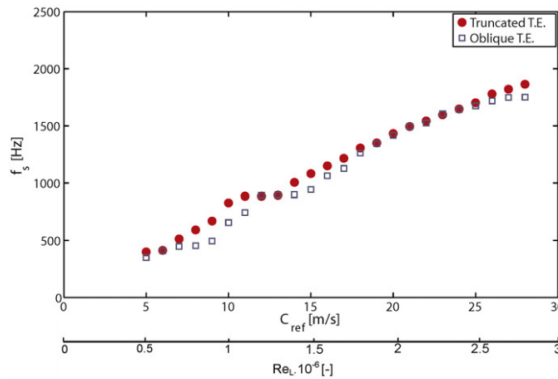


Figure 2.2: Vortex shedding frequency versus reference velocity, C_{ref} . Experimental result for a truncated and oblique trailing edge. Lock-in is occur around 10-15 m/s [3].

Zobeiri et al. [3] investigated two NACA 0009 hydrofoils, one with a blunt trailing edge and another with an oblique trailing edge. They performed the experiment in a similar Reynolds number range as Ausoni et al. [18]. Based on their vibration measurements, they confirmed that flow induced vibration was considerably reduced with an oblique trailing edge shape compared with a truncated hydrofoil. They concluded that this was caused by the collision between the upper and lower vortex, resulting in a vorticity redistribution.

Hu et al. [19] studied vortex shedding numerically of a truncated NACA 0009 hydrofoil. They investigated the shedding characteristic under different operation conditions such as inlet velocity, angle of attack, and trailing edge thickness. Their results showed that the frequency of vortex shedding increase with inlet velocity. Their numerical result was closer to the experimental result obtained in another work by Ausoni et al. [20], where a turbulent boundary layer was promoted by a rough strip on the leading edge. The numerical results also showed the the shedding frequency was reduced by increasing the angle of attack. At a certain angle of attack, the oscillation ceased.

Lockey et al. [21] numerically studied the von Kármán vortex shedding behind a stay vane, with experimental results used for validation. They found that the numerically predicted shedding frequency was not highly dependent on the numerical grid compared to the amplitude of the shedding, which was highly influenced by the mesh. In addition, the computed frequency was not influenced by the turbulence model, but the predicted amplitude showed a strong dependence.

There have been conducted several studies on the von Kármán vortex shedding. There are, however, to the author's knowledge, no study that investigates the interaction between the corner vortex and the trailing edge vortex in hydraulic turbines.

Chapter 3

Theory

3.1 Vorticity

Vortex structures, which is also named secondary flow structures is associated with the rotating motion of fluid around a center line. These structures originates from the boundary layer vorticity of a flow that passes through a curved duct.

$$\boldsymbol{\omega} = \nabla \times \mathbf{u} \quad (3.1)$$

The vorticity vector is defined in Equation 3.1. The vorticity vector is a measure of rotation of a fluid particle. If the vorticity at a point in a flow field is nonzero, the fluid particles that occupy that point in space are rotating. Thus, flow in that region is characterized as rotational. Similarly, if the vorticity in a region is zero or negligibly small, the fluid particles within this region are not rotating, thereby the flow in this region is called irrotational [22]. For example, flow within the viscous boundary layer near a wall is considered rotational, while fluid particles outside the boundary layer are irrotational.

The components of the vorticity vector is calculated as the sum of the rotation rate of two mutually perpendicular fluid lines. Therefore, considering a mono-directional flow as depicted in Figure 3.1. The velocity profile of the boundary layer consist of one vorticity component, i.e. the component perpendicular to the streamwise direction. As the velocity along the x direction gradually increase from the wall and the streamlines are parallel, the vorticity component is as shown in Equation 3.2.

$$\omega_z = \frac{\partial v}{\partial x} - \frac{\partial u}{\partial y} \approx -\frac{\partial u}{\partial y} \quad (3.2)$$

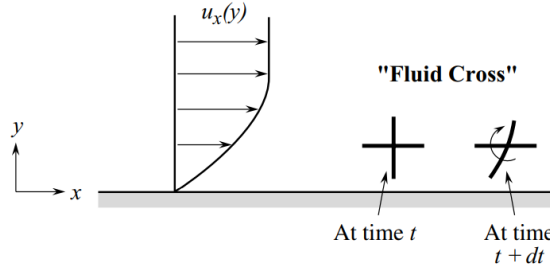


Figure 3.1: Rotation of fluid element in a mono-directional shear flow [4].

Where u and v denotes the x-component and y-component of the velocity vector, respectively. Moreover, substituting Equation 3.2 into the shear stress relation for a Newtonian fluid gives:

$$\tau_{x,y} = \mu \frac{\partial u}{\partial y} = -\mu \omega_z \quad (3.3)$$

Furthermore, the described relation above can be substituted into the momentum equation for the boundary layer, yielding:

$$\frac{1}{\rho} \frac{\partial p}{\partial x} = \nu \frac{\partial^2 u}{\partial y^2} \Big|_{y=0} = -\nu \frac{\partial \omega_z}{\partial y} \Big|_{y=0} \quad (3.4)$$

Equation 3.4 show that vorticity is developed from the no-slip condition at the wall and is diffused in the direction normal to the wall, as result of the streamwise pressure gradient.

In order to make real use of vorticity as a framework for the physical interpretation and qualitative understanding of fluid phenomena, it is necessary to consider how different physical factors affect the dynamics of vorticity.

An equation for the rate of change of vorticity is obtained from the governing equation for fluid motion, which is written in a general form in Equation 3.5.

$$\frac{\partial \mathbf{u}}{\partial t} + \mathbf{u} \cdot \nabla \mathbf{u} = -\frac{1}{\rho} \nabla p + \mathbf{X} + \mathbf{F}_{visc} \quad (3.5)$$

Here \mathbf{X} denotes the volume forces and \mathbf{F} are the viscous forces acting on the fluid element. The equation for vorticity is derived by taking the curl of Equation 3.5

[4]:

$$\frac{D\omega}{Dt} = \frac{\partial\omega}{\partial t} + (\mathbf{u} \cdot \nabla)\omega = (\omega \cdot \nabla)\mathbf{u} - \omega(\nabla \cdot \mathbf{u}) - \nabla \times \left(\frac{1}{\rho} \nabla p\right) + \nabla \times \mathbf{X} + \nabla \times \mathbf{F}_{visc} \quad (3.6)$$

Where the terms are:

- $\frac{\partial\omega}{\partial t}$ describes the rate change due to a unsteady vorticity field.
- $(\mathbf{u} \cdot \nabla)\omega$ describes the rate of change due to convection.
- $(\omega \cdot \nabla)\mathbf{u}$ is the stretching and tilting due to velocity gradients.
- $\omega(\nabla \cdot \mathbf{u})$ accounts for compressibility effects.
- $\nabla \times \left(\frac{1}{\rho} \nabla p\right)$ describes vorticity production due a pressure gradient imposed on a fluid particle with non-uniform density distribution.
- $\nabla \times \mathbf{X}$ describes change in vorticity due to body forces.
- $\nabla \times \mathbf{F}_{visc}$ is related to viscous diffusion of vorticity.

For the fluid flow considered in this study, the flow is incompressible, viscous, and with no body forces. Thus, Equation 3.6 becomes:

$$\frac{D\omega}{Dt} = \frac{\partial\omega}{\partial t} + (\mathbf{u} \cdot \nabla)\omega = (\omega \cdot \nabla)\mathbf{u} + \nabla \times \mathbf{F}_{visc} \quad (3.7)$$

There are two terms in Equation 3.7, one accounts for tilting and stretching, the second term describes the change in vorticity due to viscous effects. The former mentioned is responsible for the creation of vorticity components due to the non-uniform convection rate of different parts of a vortex line, giving rise to the so-called secondary flow that occurs in a turbomachinery passage. This effect is illustrated in Figure 3.2, where the vorticity is visualized as a vortex line that is entering with its boundary layer vorticity normal to the streamwise flow. As the flow turns, the fluid particle on the outside will travel with a lower velocity, for a longer distance compared to those on the inside [4]. As a consequence, the vortex line that was initially normal to the free stream, ends up oriented at the passage exit. Hence, a streamwise vorticity component is generated because of the velocity gradient across the duct.

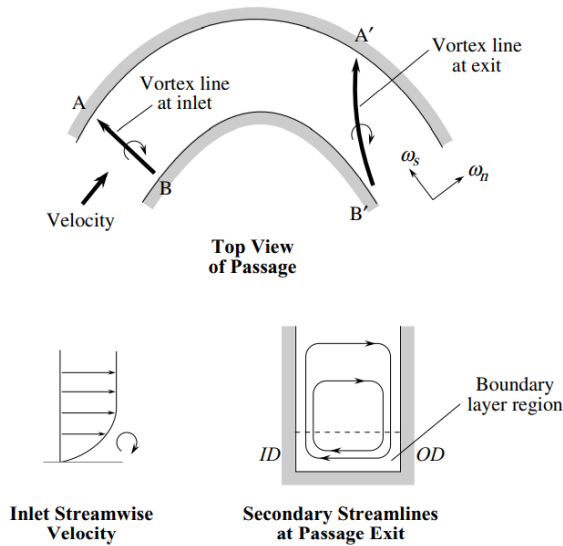


Figure 3.2: Generation of streamwise vorticity component (secondary flow) from convection of vortex lines [4].

Secondary flows usually occur in turbomachinery cascades, as a consequence of endwall vorticity being convected through a bladed channel. Therefore, the flow in turbomachinery is highly three dimensional, which is characterized by various vortical structures. In the following section, a few secondary flow structures will be presented.

3.2 Secondary flow

There is a wide variety of secondary flow structures that occurs in a turbine passage. Throughout the years, secondary flow structures have been under extensive research with respect to highly loaded turbine cascades featuring low aspect ratios and thickness-chord ratios. In high pressure turbines such as a gas turbine or those commonly used for the first stages, the aerodynamic losses or secondary flow losses can be as high as 30-50% of the total pressure losses according to Sharma and Butler [23].

Different models of secondary flow have been presented throughout the years, with various reports on the inception and interaction of vortical structures within the passage. However, the most fundamental secondary flow phenomena such as the

endwall crossflow, horseshoe vortex, and passage vortex are generally agreed upon and will be presented [24]. As mentioned these vortical structures are known to appear in highly loaded turbine cascades with low aspect ratios. However, in the context of hydraulic axial turbines, some of these secondary structures may not appear as a prominent feature within the passage flow, as hydraulic turbine tend to operate with greater aspect ratios and chord lengths. Nevertheless, the underlying physics regarding vortex development and interaction is the same, and will therefore be presented as similar vortex structures appear in the present work.

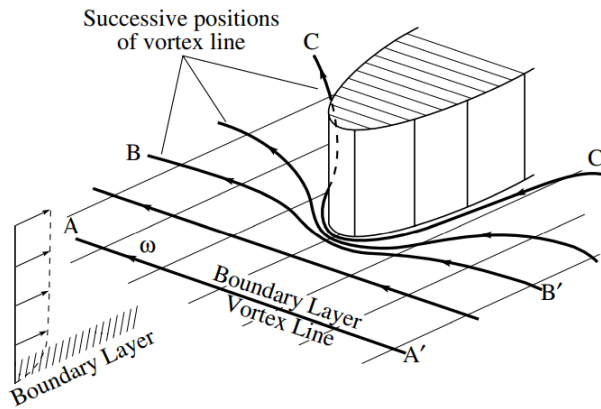


Figure 3.3: Boundary layer vortex lines wrapping around leading edge [4].

A frequently encountered vortical phenomenon in fluid applications is the well known horseshoe vortex. This phenomenon occurs in the flow of a boundary layer around an obstacle or this case a blade that protrudes through it. As the flow approaches the leading edge, the upstream boundary layer separate due to an adverse pressure gradient near the leading edge. This causes the flow to roll up and wrap itself around the blade resulting in two vortex structures. Furthermore, the phenomenon can be visualized as boundary layer vortex lines, as depicted in Figure 3.3. From Figure 3.3, it can be observed that the phenomenon give rise to streamwise vorticity, because of vorticity stretching as explained in section 3.1.

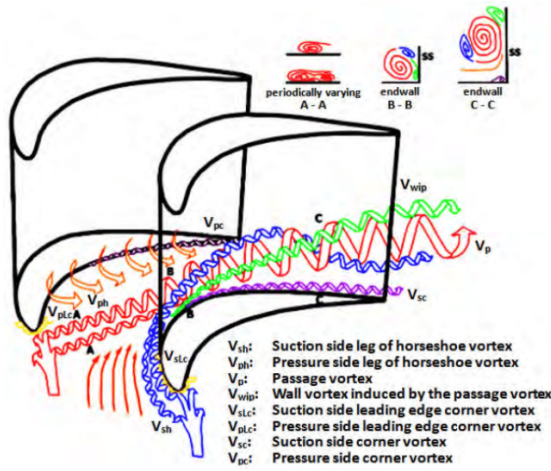


Figure 3.4: Secondary flow model by Wang et al.(1997).

In the case of a blade cascade that consists of asymmetric blades. The horseshoe vortex splits into a pressure side leg and a suction side leg, with opposite sense of rotation. The pressure side leg will propagate across the passage as it is drawn toward the suction side of the blade by pitchwise pressure gradient and the endwall crossflow. On the other hand, the suction side leg will remain close to the suction side of the blade. As the pressure side leg travels downstream, it merges with the endwall cross flow and grows in size and intensity to evolve into a vortex called the passage vortex, which then interact with vortex filaments developed on the adjacent junction between the blade wall and endwall, as depicted in Figure 3.4.

Apart from the vortex structures mentioned, there are several additional vortex structures, that can be induced by the abovementioned structures and other variables. Figure 3.4 is an example of a complex secondary flow model, but it should be noted that the flow picture depends on blade shapes and gradient of pressure. Thus, the formation of vortical structure will vary from cascade to cascade.

3.3 Frequency of vortex shedding

The frequency of vortex formation for cylinder has been found to follow Strouhal's empirically derived relation [22]:

$$f = \text{St} \frac{U}{D} \quad (3.8)$$

Where St denotes the dimensionless Strouhal number, f is the frequency of vortex shedding, U is the free stream velocity and D is the projected cross sectional dimension on the approaching flow, determined as the cylinder diameter.

Several studies have found the Strouhal number to be a function of the Reynolds number for a circular cylinder. In Figure 3.5, the Strouhal number is plotted against the Reynolds number. The Strouhal number remains relatively constant for a wide range of Reynolds numbers, as shown in Figure 3.5. In the range of $10^3 \leq Re \leq 10^5$, where it is nearly constant, the Strouhal number can often be approximated as 0.2.

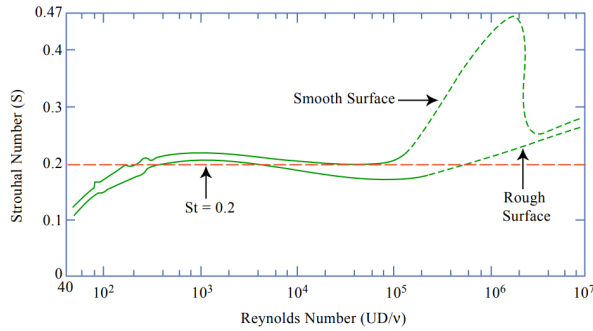


Figure 3.5: Relationship between Strouhal number and Reynolds number for circular cylinders [5].

Although Strouhal's formula proved to be valid for flow across bluff objects, it is not applicable to flow across slender objects such as turbine blade. For flow induced vibration on hydrofoils, Gongwer [25], Donaldson [26], and Heskestad/Olberts [2] investigated the effect of trailing edge geometry on shedding dynamics and resulting structural vibration.

In the study by Gongwer [25], the trailing edge thickness was investigated. Gongwer suggested a modification of Strouhal's formula in the dimension, D , which was chosen as the sum of the trailing edge thickness and an experimentally determined fraction of the boundary layer displacement thickness. His correction to the Strouhal formula is presented in Equation 3.9 [25].

$$f = St \frac{U}{(t + \delta_v)} \quad (3.9)$$

Where t is the trailing edge thickness in unit millimetres. δ_v denotes the virtual

boundary layer, which is defined as a fraction of 0.643 of the displacement thickness of a turbulent boundary layer:

$$\delta_v = 0.643 \frac{1}{8} \frac{0.37c}{\text{Re}^{\frac{1}{5}}} \quad (3.10)$$

c is the chord length of the blade, and Re is the chord based Reynolds number. Gongwer also found the Strouhal number to be constant and equal to 0.19 for a range of Reynolds number.

Opposed to Gongwer's consideration of excluding the effect of trailing edge geometry, Donaldson [26] presented a detailed study on a wide variety of trailing edges on the same blade. In this study, he focused on the magnitude of vortex induced forces. From the experiment, it was found that modification to the trailing edge significantly reduced the amplitude of vibration of the blade, while the frequency remained relatively unchanged. Oblique, truncated, symmetrically tapered, and cavity edges were investigated in his study. The asymmetrical shapes displayed a significant reduction while the symmetrical ones amplified the vibration. Additional research carried out by Donaldson show a substantial reduction in the amplitude of vibration using the so called Donaldson cut consisting of a combination of a straight 45° cut and a third order polynomial curve.

Based on the work of Donaldson, Heskestad and Olberts [2] conducted additional experiment on the same trailing edge shapes, with a detailed study on the variation of angles for the different geometries. As mentioned in chapter 2, the vortex shedding frequency was found to be highly influenced by the trailing edge geometry. As a correlation was found between the shedding frequency and trailing edge shape, a modified Strohaul formula was presented, to include the effect from the trailing edge geometry, as shown in the following equation:

$$\text{St} = \frac{100}{B} \frac{f(t + \delta_v)}{U} \quad (3.11)$$

Where B is a constant determined by the trailing edge geometry. Figure 3.6 show the value related to the different trailing edge shapes, which also show the relative amplitude of vibration, A , compared to the truncated trailing edge.

In the work of Brekke [6], Equation 3.11 is presented with a constant virtual boundary layer displacement thickness of 0.56 mm and a Strouhal number of 0.19 in the following equation:

$$f = 190 \frac{B}{100} \frac{U}{t + 0.56} \quad (3.12)$$

The above mentioned empirical formulas for estimation of vortex shedding frequency and the Strouhal number, are derived from research using simplified hydrofoils. As depicted in Figure 3.6, measurements are based on rectangular geometries upstream of the trailing edge, that have parallel upper and lower surfaces. This is not the case for an actual blade in hydraulic turbomachinery. Furthermore, neither of the empirically derived formulas consider different angles of attack and three dimensional effects from the flow. However, these empirical formulas may be used as a comparative tool for data acquired through simulation or experiments.

	A	B		A	B
	100 (100)	100		(0)	
	(48)			(0)	
	38 (20)	112		190 (230)	96
	3 (0)	131		380 (360)	93
	0	149		43	117
	0	181		0	159
	(260)			31 (43)	103

Figure 3.6: Trailing edge of hydrofoil with relative amplitude A and value of geometrical constant B [6].

3.4 Turbulence

Most flow encountered in real life are turbulent. The flow regime is described as an irregular state of flow in which physical quantities like velocity, pressure, temperature and vorticity vary almost randomly in space and time. This is a three-dimensional phenomenon observed at higher Reynolds numbers. At lower Reynolds numbers flow are laminar. The Reynolds number is a dimensionless quantity given by:

$$\text{Re} = \frac{UL}{\nu} \quad (3.13)$$

where U is the characteristic velocity, L is the length scale of the mean flow and ν is the kinematic viscosity. Equation 3.13 describes the ratio between inertial forces and viscous forces.

The characteristic structures visible in a turbulent flow are rotational structures, these are called turbulent eddies. These fluctuate on a broad range of length and time scales. Larger length scale are comparable to the size of flow boundaries, whereas the smallest are in the order of 0.1 to 0.01 mm [27]. The smallest scale are named after Kolomogorov a Russian scientist who carried out groundbreaking research on turbulent structures. A Reynold number based on the kolomogrov microscale is equal to 1, thus smaller eddies dissipate due to viscous stresses. Smaller eddies are created by larger eddies which in turn interact and extracts energy from the mean flow. This process of energy transfer from the mean kinetic energy to progressively smaller and smaller eddies is termed the energy cascade.

3.5 Computational fluid dynamics

A CFD software is used in this study to simulate fluid flows. In a CFD software the equation governing the dynamic of fluid motion are solved. These equations are nonlinear partial differential equations, and have no analytical solution. Hence, a numerical algorithm is implemented in the CFD software to find a solution by an iterative method. The CFD software used in this study, discretize the equation numerically by the finite volume method. A numerical grid (mesh) representing a fluid domain is created where each cell express the relevant conservation properties of the equations. The accuracy of the numerically obtained solution is governed by the number of element in the mesh. The larger the number of element, the better the solution accuracy. However, larger number of cells comes at the cost of increased computation time. An optimal mesh is therefore finer in areas with large gradients, and coarser in areas with little change.

The governing equations of fluid motion represents the conservation laws of physics. These are the conservation of mass and Newtons' second law, which are known as the continuity and Navier-Stokes (N-S) equation, respectively. The flow quantities are in Cartesian coordinates where the velocity vector \mathbf{u} is composed of x -component u , y -component v and z -component w . For an incompressible flow, where density ρ is constant, the continuity and the Navier-Stoke equations are presented in Equation 3.14 and Equation 3.15-3.17, respectively [27].

$$\operatorname{div}(\mathbf{u}) = 0 \quad (3.14)$$

$$\frac{\partial u}{\partial t} + \operatorname{div}(u\mathbf{u}) = -\frac{1}{\rho} \frac{\partial p}{\partial x} + \nu \operatorname{div}(\operatorname{grad}(u)) \quad (3.15)$$

$$\frac{\partial v}{\partial t} + \operatorname{div}(v\mathbf{u}) = -\frac{1}{\rho} \frac{\partial p}{\partial y} + \nu \operatorname{div}(\operatorname{grad}(v)) \quad (3.16)$$

$$\frac{\partial w}{\partial t} + \operatorname{div}(w\mathbf{u}) = -\frac{1}{\rho} \frac{\partial p}{\partial z} + \nu \operatorname{div}(\operatorname{grad}(w)) \quad (3.17)$$

In the N-S equation ν denotes the kinematic viscosity, t stands for time and p stands for pressure. Body forces are not expressed in the equations.

In a statistically steady flow, every variable can be decomposed into the sum of a time-averaged value and a fluctuation about that value [28]:

$$\phi(x_i, t) = \bar{\phi} + \phi'(x_i, t) \quad (3.18)$$

$$\bar{\phi}(x_i) = \lim_{T \rightarrow \infty} \int_0^T \phi(x_i, t) dt \quad (3.19)$$

t is the time and T is the averaging interval. If the interval is large enough compared to the time scale of the fluctuations, i.e. T gets to infinity, then $\bar{\phi}$ does not depend on the time at which the averaging started.

If the flow is unsteady, time averaging cannot be used. In order to describe the time-dependent mean value, ensemble averaging must be used.

$$\overline{\phi(x_i, t)} = \lim_{N \rightarrow \infty} \frac{1}{N} \sum_{n=1}^N \phi(x_i, t) \quad (3.20)$$

Where N is the number of members of the ensembles and must be sufficiently large to eliminate the effects of fluctuations. The equations presented in the above represent a way of handling turbulence. This is done by applying the averaging processes presented above to the continuity and N-S equations, which will yield the Reynolds-Average Navier-Stokes equations (RANS). It can be derived by using the decomposition method in Equation 3.18 to the continuity and N-S equation by replacing the flow variables \mathbf{u}, u, v, w , and p by the sum of a mean and fluctuating component:

$$\mathbf{u} = \mathbf{U} + \mathbf{u}' \quad u = U + u' \quad v = V + v' \quad w = W + w' \quad p = P + p' \quad (3.21)$$

Then the time average is taken, thus it yields the continuity equation for the mean flow:

$$\text{div}(\mathbf{U}) = 0 \quad (3.22)$$

and time average for x -, y -, and z -momentum equations ([27],p.95):

$$\begin{aligned} \frac{\partial U}{\partial t} + \text{div}(U\mathbf{U}) = & -\frac{1}{\rho} \frac{\partial P}{\partial x} + \nu \text{div}(\text{grad}(U)) \\ & + \frac{1}{\rho} \left[\frac{\partial(-\overline{\rho u'^2})}{\partial x} + \frac{\partial(-\overline{\rho u'v'})}{\partial y} + \frac{\partial(-\overline{\rho u'w'})}{\partial z} \right] \end{aligned} \quad (3.23)$$

$$\begin{aligned} \frac{\partial V}{\partial t} + \text{div}(V\mathbf{U}) = & -\frac{1}{\rho} \frac{\partial p}{\partial y} + \nu \text{div}(\text{grad}(V)) \\ & + \frac{1}{\rho} \left[\frac{\partial(-\overline{\rho v'^2})}{\partial x} + \frac{\partial(-\overline{\rho v'u'})}{\partial y} + \frac{\partial(-\overline{\rho v'w'})}{\partial z} \right] \end{aligned} \quad (3.24)$$

$$\begin{aligned} \frac{\partial W}{\partial t} + \text{div}(W\mathbf{U}) = & -\frac{1}{\rho} \frac{\partial p}{\partial z} + \nu \text{div}(\text{grad}(W)) \\ & + \frac{1}{\rho} \left[\frac{\partial(-\overline{\rho w'^2})}{\partial x} + \frac{\partial(-\overline{\rho w'u'})}{\partial y} + \frac{\partial(-\overline{\rho w'v'})}{\partial z} \right] \end{aligned} \quad (3.25)$$

The process of time-averaging has introduced a new term in the N-S equation. The new terms appear inside the brackets and can be written in tensor notation as:

$$\overline{\rho u'_i u'_j} \quad (3.26)$$

The new term represent six additional turbulent stresses in the RANS Equation. These are also called the Reynolds stresses. The presence of the Reynold stresses in RANS equations means that the equation set are not closed. This implies that there are more variables than equations. Hence, turbulence models are used to model the turbulent stresses in order to close the set of equation.

3.6 Turbulence models

The three most commonly used branches of turbulence modelling are RANS, large eddy simulation (LES), and direct numerical simulation (DNS). LES and DNS models are accurate at predicting turbulence, but calculations are highly costly in

terms of computing resources, so the method is mainly used for the purpose of research.

RANS models are considered to be the standard for general applications due to speedy solution. The computing resources needed for a reasonable accurate flow are modest. These models have been developed to model the Reynolds stresses, so the system of equation can be closed. The most used and validated RANS turbulence models are $k - \epsilon$, $k - \omega$, and SST $k - \omega$. These models are two equation models, thus two equations are solved in addition to the RANS equations.

In the $k - \epsilon$ model one transport equation is solved for turbulent kinetic energy $k = \frac{1}{2}u'_i u'_i$, and another for the dissipation rate of turbulent energy ϵ . The $k - \omega$ model is similar to the $k - \epsilon$ model, but it uses the turbulence frequency $\omega = \epsilon/k$ as the second variable ([27], p.90). The simulations conducted in the present work have been performed with the SST $k - \omega$ model and the SST-SAS model. These are presented below.

Menter's shear stress transport (SST) $k - \omega$ model, is a combination of the $k - \epsilon$ model and $k - \omega$ model. This hybrid model uses a transformation of the $k - \epsilon$ into a $k - \omega$ in the near-wall region and the standard $k - \epsilon$ in the fully turbulent region far from the wall. Combining these two model, one can utilize the strength from both models. The $k - \epsilon$ model is less sensitive to assumed values in the free-stream, but has an unsatisfactory near-wall performance for boundary layers with adverse pressure gradients. While the $k - \omega$ show superior performance for adverse pressure gradient boundary layer, but is on the other hand highly sensitive to turbulent properties in the free-stream. This model computes the Reynold stress with the Boussinesq expression ([27],p.90):

$$-\overline{\rho u'_i u'_j} = 2\mu_t S_{ij} - \frac{2}{3}\rho k \delta_{ij} = \mu_t \left(\frac{\partial U_i}{\partial x_j} + \frac{\partial U_j}{\partial x_i} \right) - \frac{2}{3}\rho k \delta_{ij} \quad (3.27)$$

$$S_{ij} = \frac{1}{2} \left(\frac{\partial U_i}{\partial x_j} + \frac{\partial U_j}{\partial x_i} \right) \quad (3.28)$$

Where μ_t is the eddy viscosity, δ_{ij} is the Kronecker delta ($\delta_{ij} = 1$ if $i = j$ and $\delta_{ij} = 0$ if $i \neq j$), and S_{ij} is the mean rate of strain. The turbulent kinetic energy appear in Equation 3.27, and is described in the following equation:

$$\frac{\partial(\rho k)}{\partial t} + \text{div}(\rho k \mathbf{U}) = \text{div} \left[\left(\mu + \frac{\mu_t}{\sigma_k} \right) \text{grad}(k) \right] + P_k - \beta^* \rho k \omega \quad (3.29)$$

$$P_k = \left(2\mu_t S_{ij} S_{ij} - \frac{2}{3}\rho \frac{\partial U_i}{\partial x_j} \delta_{ij} \right) \quad (3.30)$$

Here, P_k denotes the production term. The second transport equation is derived from the ϵ -equation, which is transformed into a ω -equation by substituting $\epsilon = k\omega$. Leading to the following equation:

$$\begin{aligned} \frac{\partial(\rho\omega)}{\partial t} + \text{div}(\rho\omega\mathbf{U}) = \text{div} \left[\left(\mu + \frac{\mu_t}{\sigma_{\omega,1}} \right) \text{grad}(\omega) \right] \\ + \gamma_2 \left(2\rho S_{ij} S_{ij} - \frac{2}{3}\rho\omega \frac{\partial U_i}{\partial x_j} \delta_{ij} \right) - \beta_2 \rho\omega^2 + 2 \frac{\rho}{\sigma_{\omega,2}\omega} \frac{\partial k}{\partial x_k} \frac{\partial \omega}{\partial x_k} \end{aligned} \quad (3.31)$$

σ_k , $\sigma_{\omega,1}$, $\sigma_{\omega,2}$, γ_2 , β and β^* are model constants. Since it was first introduced in 1992, a number of modifications have been implemented to optimise the performance. One of the improvement is the use of blending function to achieve a smooth transition between the two models. Furthermore, eddy viscosity and the turbulent kinetic energy production are limited to prevent build-up of turbulent properties.

The shear stress transport-scale adaptive simulation (SST-SAS) model represent a new approach among the unsteady RANS (URANS) models. Contrary to the standard RANS formulation, the SAS model adjusts the turbulent length scale to local flow instabilities. To measure the local flow length scale, the well known von Kármán length scale L_{vK} is introduced into the ω -transport equation [29]. The von Kármán length scale allow the model to react more dynamically to resolved scales in the flow which can not be handled by standard URANS models.

The SST-SAS model provides a steady state solution in stable flow regions, and captures unsteady flow by reducing its eddy viscosity according to the locally resolved vortex size represented by the von Kármán length scale. Thereby, it can resolve the turbulent spectrum down to the grid limit, as illustrated in Figure 3.7. For a detailed breakdown of the SST-SAS, the reader is recommended to look in [7].

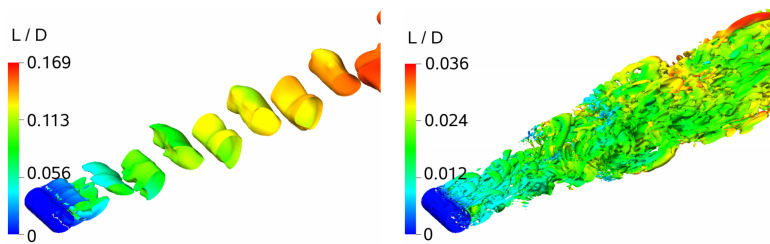


Figure 3.7: Cylinder in cross flow at Reynolds number of $3 \cdot 10^6$. Left: URANS. Right: SAS [7].

Chapter 4

Numerical method

4.1 Model description

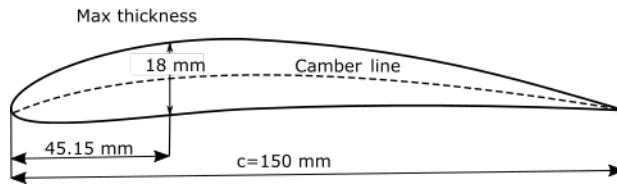


Figure 4.1: NACA 6412.

The numerical simulation in this master thesis are based on the NACA 6412 profile, which is a design commonly found in kaplan turbines. The first digit denotes a maximum camber of 6% of the chord (hydrofoil length), the second indicates the position of the maximum camber as 40% of the chord, and the last two digit specifies that maximum thickness of the hydrofoil is 12% of the chord. Furthermore, the chord length, c , was selected to be 150 mm, as shown in Figure 4.1. The coordinates for the entire hydrofoil is computed using the the following equations [30]:

$$y_c = \begin{cases} 0.06 \frac{x}{p^2} \left(2 \cdot 0.4 - \frac{x}{c} \right), & 0 \leq x \leq 0.4c \\ 0.06 \frac{c-x}{(1-p)^2} \left(1 + \frac{x}{c} - 2 \cdot 0.4 \right), & 0.4c \leq x \leq c \end{cases} \quad (4.1)$$

Equation 4.1 computes the mean camber line coordinates by plugging in values of x from 0 to maximum chord c . The thickness distribution above and below the mean line has to be calculated from Equation 4.2.

$$\pm y_t = 0.12c^5 \left[0.2969 \sqrt{\frac{x}{c}} - 0.1260 \frac{x}{c} - 0.3516 \left(\frac{x}{c}\right)^2 + 0.2843 \left(\frac{x}{c}\right)^3 - 0.1015 \left(\frac{x}{c}\right)^4 \right] \quad (4.2)$$

The final coordinates for the upper surface (x_u, y_u) and lower surface (x_l, y_l) are obtained by the following relationships:

$$x_u = x - y_t \sin \theta \quad y_u = y_c + y_t \cos \theta \quad (4.3)$$

$$x_l = x + y_t \sin \theta \quad y_l = y_c - y_t \cos \theta \quad (4.4)$$

where θ is:

$$\theta = \arctan\left(\frac{dy_c}{dx}\right) \quad (4.5)$$

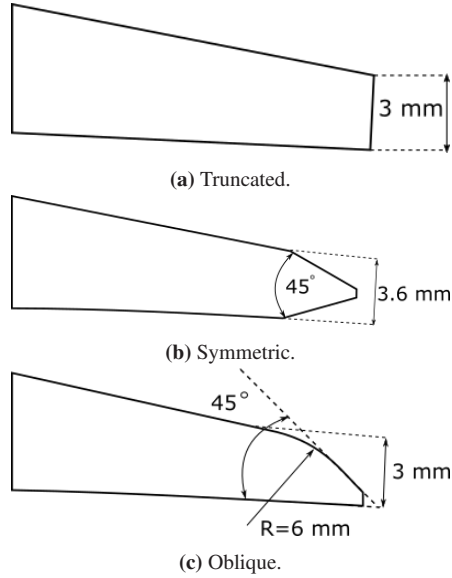


Figure 4.2: Trailing edge geometry.

In order to investigate the dynamic of the trailing edge vortex and its interaction with the corner vortex, simulations have been performed for different operating

condition. Thus, simulation has been conducted for three different trailing edges and three angles of attack, resulting in total of 9 simulations. The three trailing edge shapes designed are sketched in Figure 4.2. One trailing edge is truncated, the second has a oblique trailing edge, and the last shape is symmetrical. The selected geometries were inspired by shapes used in Brekke's [6] investigation of trailing edge shapes, as illustrated in Figure 3.6. These trailing edges were created in a three-dimensional computer aided design software (CAD), where ten percent of the chord from the trailing edge of the NACA 6412 was modified in order to alter the geometry into the shapes shown in Figure 4.2.

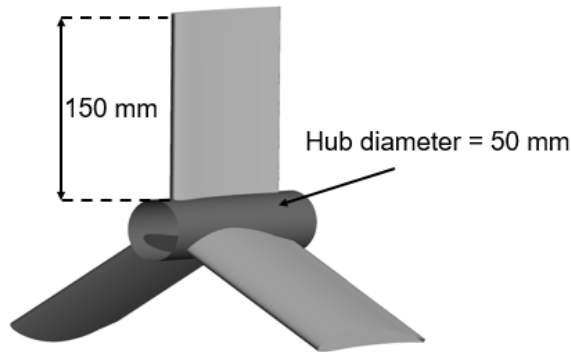


Figure 4.3: Radial cascade geometry.

The radial cascades were created with three hydrofoils, as depicted in Figure 4.3. The dimension for the span-wise length of the hydrofoil was set to 150 mm. The dimension of hub diameter and shroud diameter are 50 mm and 350 mm, respectively. Furthermore, the hub was extended 20 mm upstream from the leading edge, and 35 mm downstream of the trailing edge. As mentioned, simulations were run for three angles of attack, $\alpha = 0^\circ$, 3° , and 6° . In order to avoid hydrofoils from touching each other at $\alpha = 6^\circ$, the hydrofoil chord length was limited to 150 mm, after testing different chord lengths.

4.2 Meshing approach

The numerical meshes were constructed in ANSYS turbogrid, and consists approximately of 6 million elements, respectively. Here, complex blade models can automatically be produced into high quality meshes, i.e. structured and composed of hexahedral elements. To use Ansys turbogrid, one can either define a geometry from a CAD source or profile points. The latter option was used in this case, where

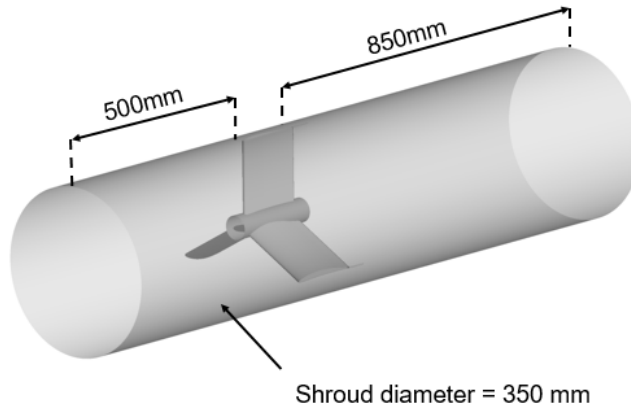


Figure 4.4: Numerical model of radial cascade.

separate curve (.crv) files for the hub, shroud and blade were loaded into ANSYS turbogrid [31]. These curve files contain the coordinate data points that define the geometry and are given in Appendix A.

Since the radial cascade was axisymmetric, it allowed for a reduction in the number of mesh elements. Consequently, leading to a considerable reduction of computation time. Hence, numerical simulations were conducted only for one blade passage, as depicted in Figure 4.5. Ideally, its recommended to design the length of inlet from the leading edge 10 times the pipe diameter. This condition, however, was not satisfied due to limited time and computation power. Therefore the inlet length was limited to 500 mm upstream of the leading edge. On the other hand, the outlet was extended 850 mm downstream of the trailing edge, to avoid effects of the boundary. Typically, the outlet has a greater effect than the inlet boundary, because of the downstream vortex shedding. Hence, the hydrofoil was further away from the outlet than from the inlet.

Figure 4.6 shows the mesh topology around the hydrofoils with different trailing edges. The numerical grid has been created with refined boundary layers on all surfaces, including the hydrofoil. As capturing the von Kármán vortex is the primary objective, the mesh was substantially refined around the trailing edge. It should be sufficiently refined at the proximity of the trailing to resolve the physics in the immediate wake, but there may be some accuracy lost in the wake, due to larger cells with a high aspect ratio. This inaccuracy will further be inspected and addressed in subsection 4.3.3

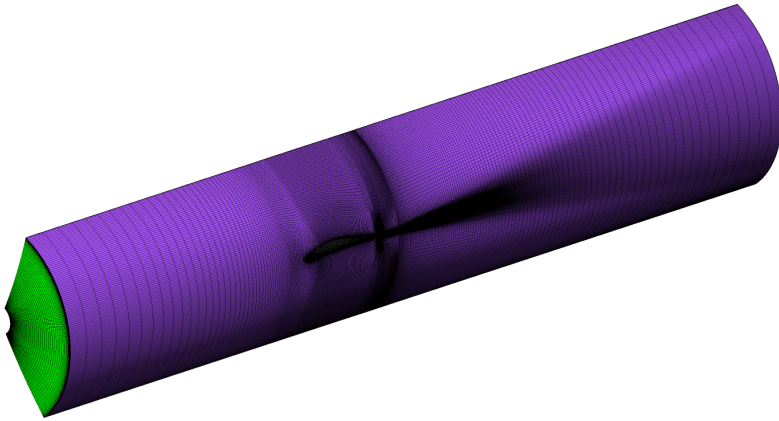


Figure 4.5: Numerical grid of blade passage.

In a flow that is characterised as turbulent, physical variables usually vary most considerably around the boundaries. Thus, it is important to resolve the boundary layer without utilizing wall functions in the computation. Therefore, the hydrofoil boundary layer was resolved with y^+ value below 1, which yielded a first layer thickness of $8.5 \cdot 10^{-6}$ m, except at the very end of the trailing edge where the flow is assumed to be separated. In this region, y^+ becomes a value of 4. The expansion rate of the layers was set to 1.3, and the boundary layers were comprised with a total of 10 layers. A similar configuration of the boundary layer was applied at the hub and shroud with a maximal y^+ value of 1.4 and 1.5, respectively. Figure 4.7 illustrate the cell distribution along the hydrofoil span.

4.3 Numerical setup

The physics and boundary conditions for the numerical models were selected in the pre-processor CFX-Pre, before simulations were run in the CFX-Solver. Most of the basic numerical settings applied in CFX-Pre are summarized in Table 4.1. Some of the applied parameters and options for the numerical setup are further described in detail below.

4.3.1 Physics and boundary conditions

The boundary conditions imposed on the numerical domain is illustrated in Figure 4.8. The inlet boundary condition was inlet velocity of 2 m/s, with medium

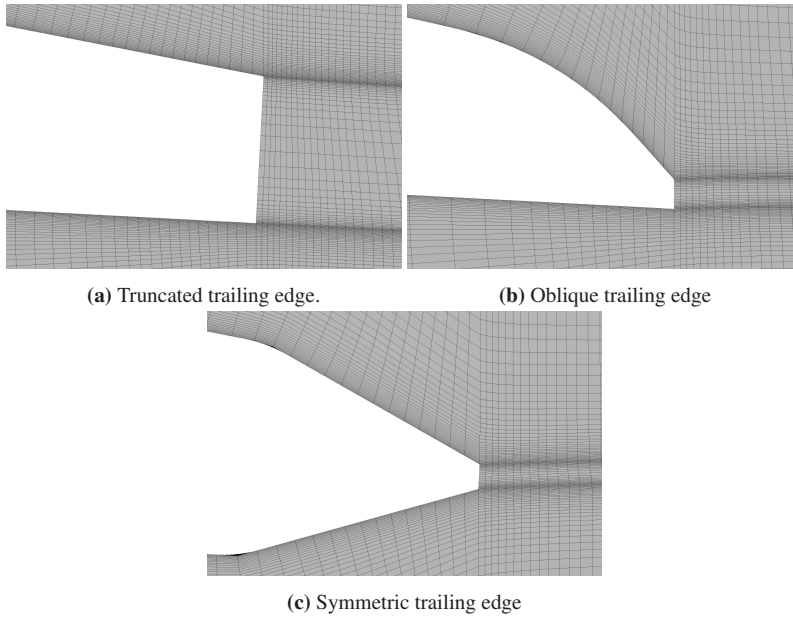


Figure 4.6: Mesh topology around trailing edge.

turbulence of 5%. Thus, giving a chord based Reynolds number of 306 000, which may be considered low compared to Reynolds numbers encountered in hydraulic turbines and previous research conducted on hydrofoils. Nevertheless, simulation were conducted on this Reynolds number to ensure a fair balance between computation time and solution quality. As increasing the velocity, would result in unsatisfactory values of the Courant number. The outlet boundary condition was set 0 Pa in relative pressure. To simulate the blade passage, periodic boundary conditions were imposed on each side of the flow passage. The shroud, hub and hydrofoil surfaces were set as smooth walls with the no-slip condition. As the numerical domain contain a hub that is hollow throughout the model, free-slip were applied on the extended hub surface upstream and downstream from the hydrofoil.

4.3.2 Timestep

To resolve the unsteady nature of vortex shedding, a sufficiently small time step must be chosen. According to Vu et al. [32], it is recommended approximately 100 time steps during one vortex shedding period to resolve the phenomenon correctly. However, this also requires an adequately fine mesh. Therefore a larger time step was chosen, based on the expected shedding frequency obtained from the Strouhal

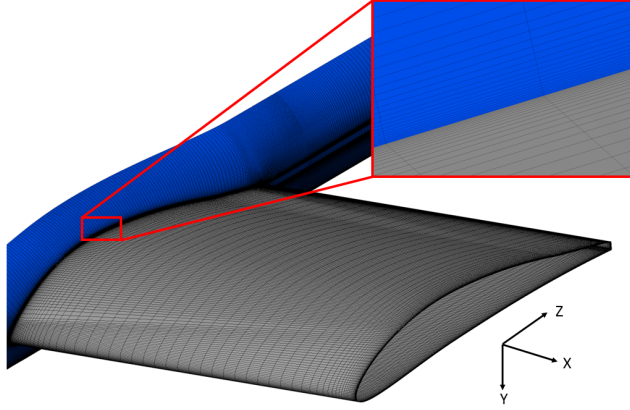


Figure 4.7: Mesh distribution along hydrofoil span.

number relation presented in section 3.3:

$$f_s = \text{St} \frac{U}{t} \quad (4.6)$$

Taking the truncated trailing edge thickness into account, $t = 3$ mm. For the chord based Reynolds number encountered in this study, the Strouhal number was chosen to be $\text{St} = 0.2$. With the velocity $U = 2$ m/s, the expected time period for one shedding is obtained from the relation:

$$T_s = \frac{1}{f_s} = \frac{t}{\text{St}U} \quad (4.7)$$

The time period will be $T_s = 7.5 \times 10^{-3}$ s. Taking this into account, a timestep of 1×10^{-4} s was chosen, which corresponded to about 75 samples per period.

4.3.3 Courant number

The Root-mean square (RMS) Courant number and max Courant number for the numerical domains was about 0.70 and 11, respectively. The max Courant number was found in the area of interest, i.e. within the thin cell layers that continue downstream from the hydrofoil surface, as depicted in Figure 4.6.

4.3.4 Turbulence model and Numerical scheme

A short overview of turbulence models was presented in section 3.6. There is a wide range of RANS models available in CFX. As mentioned, a commonly used model

Parameter	Setting
Transient scheme	Second Order Backward Euler
Advection scheme	High Resolution
Turbulence numerics	First order
Inlet velocity	$U = 2.0 \text{ m s}^{-1}$
Outlet pressure	relative pressure: 0 Pa
Time step	$\Delta t = 10^{-4} \text{ s}$
Turbulence model	SST-SAS
Convergence criteria(RMS)	10^{-4}

Table 4.1: Selected boundary condition and other parameters for the simulation.

is $k-\omega$ SST. This model has been extensively used in the prediction of trailing edge vortex. However, the SST-SAS model was used for all the simulations, with the default wall function setting called automatic. This model was selected, because of its ability to resolve a wider range of turbulent structures.

The transient simulation was ran with a Second Order Backward Euler scheme for the temporal discretization, and for the advection scheme, High Resolution was selected. The latter mentioned scheme switches between first order and second order schemes based on the local solution field to enforce the boundedness criterion. This means that in areas with low variable gradients, the blend will be closer to second order for accuracy. In areas of high gradients, the blend will be closer a first order to prevent overshoots and undershoots and maintain robustness [33]. The First Order option selected for turbulence numeric uses upwind advection and the First Order Backward Euler transient scheme.

4.4 Solution verification

To estimate the discretization error, a mesh independence test was performed according to the guidelines in the article "Procedure for Estimation and Reporting of Uncertainty Due to Discretization in CFD Applications" by Celik et al. [34]. Following the guidelines in this article, simulations were run on three significantly different meshes. Two new additional meshes were created for the mesh independence test. Based on the existing mesh, referred to as the medium mesh. A coarse mesh and a fine mesh were created. The new meshes were developed by adjusting the global size factor such that the numerical grids differ from each other by a refinement factor of 1.3. It is recommended to have a refinement factor of 1.5, but a value of 1.3 is considered sufficient according to Celik et al. [34]. The settings for the expansion rate for the surfaces were kept on a value of 1.3 for each mesh. The

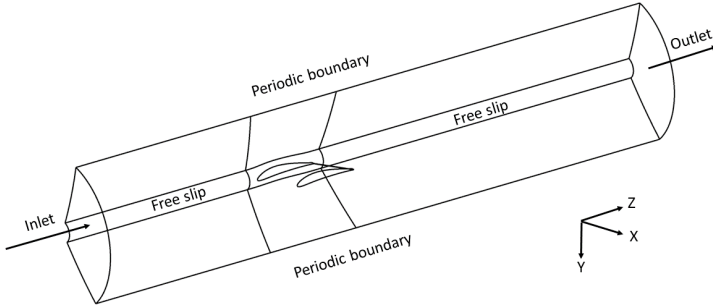


Figure 4.8: Model with boundary conditions.

simulations were run with the SST-SAS model with a time step of 10^{-4} s.

In Table 4.2, the meshes are denoted 1, 2 and 3 for the fine, medium and coarse mesh, respectively. N denotes the number of elements, r is the refinement factor, ϕ is the variable of interest, p denotes the apparent order of the method, ϕ_{ext} is the extrapolated value, e_a is the approximated error, and CGI denotes the grid convergence index.

These calculations are related to the length average of a velocity profile throughout the whole span of the hydrofoil, located 10 mm downstream of the trailing edge. The data was obtained after iterative convergence was reached for all three meshes. Based on the values obtained, the apparent order, p , was calculated to be 2.5. In ANSYS CFX, a second order accurate discretization scheme was implemented, which imply the estimated p to be in reasonable range as the desired value for a second order scheme is 2. The numerical uncertainty in the medium-grid solution for the length average of the velocity profile calculated is 11.9%.

A numerical uncertainty of 11.9% is a bit high if the mesh were to be considered mesh independent. However, when the computed shedding frequency was checked for each mesh, they predicted the same value of 120 Hz. This indicates that each mesh can be considered mesh independent concerning the frequency of vortex shedding, which is an important variable in this study. With this in mind, the medium mesh was selected, as a compromise between computation time and solution accuracy.

	Length average of velocity profile
N_1, N_2, N_3	14952600,6283104,2654942
r_{21}	1.34
r_{32}	1.33
ϕ_1	1.269 m/s
ϕ_2	1.207 m/s
ϕ_3	1.076 m/s
p	2.5
ϕ_{ext}^{21}	1.3248
e_a^{21}	4.9%
e_{ext}^{21}	4.2%
GCI_{fine}^{21}	5.47%
GCI_{course}^{32}	11.9%

Table 4.2: Discretization error estimation.

Chapter 5

Results and discussions

In this chapter, results obtained from numerical simulations are presented and discussed. A quantitative analysis of vortex shedding frequency is presented before a qualitative study of vortex interaction. The results obtained for different hydrofoil trailing edges are discussed in the following order of angle of attack, 0° , 3° , and 6° .

5.1 Vortex shedding frequency

The results obtained at zero degrees angle of attack are presented in Figure 5.1 and Figure 5.2. To investigate the flow characteristic downstream of the trailing edges, the instantaneous vorticity field is depicted on a cross-sectional plane at 50% of the blade span in Figure 5.1. In this figure, the formation of a von Kármán vortex street downstream for truncated, symmetric and oblique trailing edges are shown. As can be seen from these figures, vortices are shed alternately from the upper and lower surface of the trailing edges. Vortices appear to shed with opposite rotational direction. Vortices from the upper surface are shown as negative, while vortices from the lower surface are shown as positive. Furthermore, it is observed that the vorticity of the shed vortices dissipate as they moved downstream of the trailing edge, and the vorticity dissipation is most noticeable when the vortices first begin to separate from the trailing edge.

Figure 5.1 illustrates that there is a difference in the generation process of the von Kármán vortex street depending on trailing edge shape. However, similarity does appear for all three hydrofoils. The vortex rolled up on the upper surface is not equal in strength compared with the vortex rolled up on the lower surface. This is in contrast to the symmetrical wake and equal-strength vortices shed from the symmetrical hydrofoil with a truncated trailing edge in the work of Ausoni et al. [18]. This is caused by the asymmetry of the hydrofoil profile, which has a different

distribution of pressure on the upper and lower surface. Thus, vorticity contained within the upper shear layer is diffused into the free stream flow, due to adverse pressure gradients.

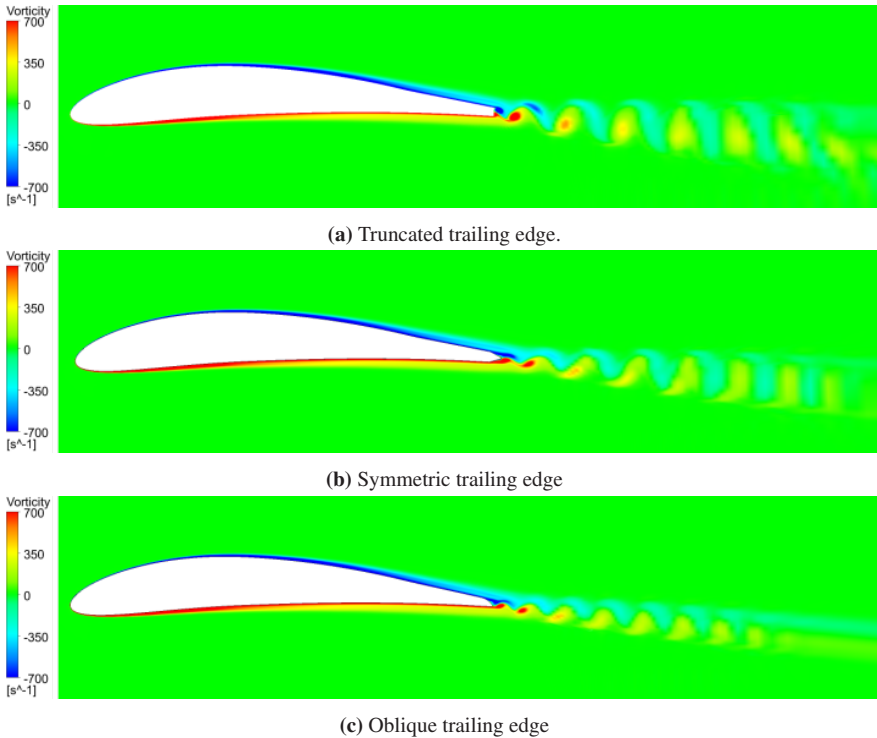


Figure 5.1: Instantaneous vorticity field at 50% span for $\alpha = 0^\circ$.

The trailing edge shape does influence the dynamic of vortex shedding. For the truncated trailing edge, there is a significant difference in the strength of the vortex in comparison to the symmetric and oblique trailing edge. Vortex cores generated from the truncated trailing edge are larger and more concentrated. When the symmetric and oblique trailing edges are compared, the former appear to have higher vortex strength as the vortices dissipate further downstream of the trailing edge. On the other hand, the oblique trailing edge, which displays the lowest vortex strength yield the highest vortex shedding frequency, which may be inferred from the longitudinal spacing between vortices.

To estimate the frequency of vortex shedding, a monitor point was placed 15 mm downstream of the trailing edge at mid-span. The velocity V (cross flow velocity)

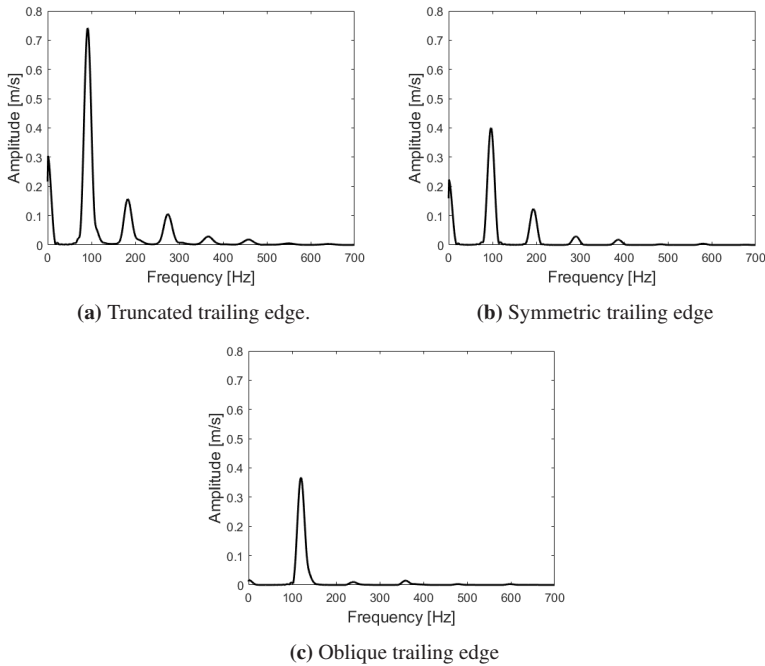


Figure 5.2: Amplitude frequency spectrum for hydrofoil trailing edges at $\alpha = 0^\circ$.

was sampled over a time interval corresponding to approximately 100 shedding periods. A fast fourier transformation (FFT) was then applied to transform velocity fluctuations to a representation in the frequency domain.

Figure 5.2 shows the amplitude frequency spectra for hydrofoils with an angle of attack of 0° . The lowest estimated frequency corresponds to the truncated trailing edge, and is 91 Hz, with an amplitude of 0.75 m/s. While the symmetric trailing edge yields the second highest frequency of 97 Hz, with an amplitude of 0.4 m/s. Lastly, the highest frequency is obtained from the oblique trailing edge, 120 Hz, with an amplitude of 0.36 m/s. The numerically predicted frequencies are consistent with previous study on trailing edge shape by Heskestad and Olberts [2], as one of many factors that influence the frequency, depend on the point of separation. Hence, the oblique trailing edge allows detachment of the boundary layer on upper surface to occur further downstream. Thus, vortex strength is significantly reduced due to upper and lower vortices almost shedding simultaneously, which results in a collision as explained by Zobeiri et al. [3]. Furthermore, the results indicate that

shedding frequency and vortex strength are inversely correlated. Thus, the higher the shedding frequency is, the lower the vortex strength will be.

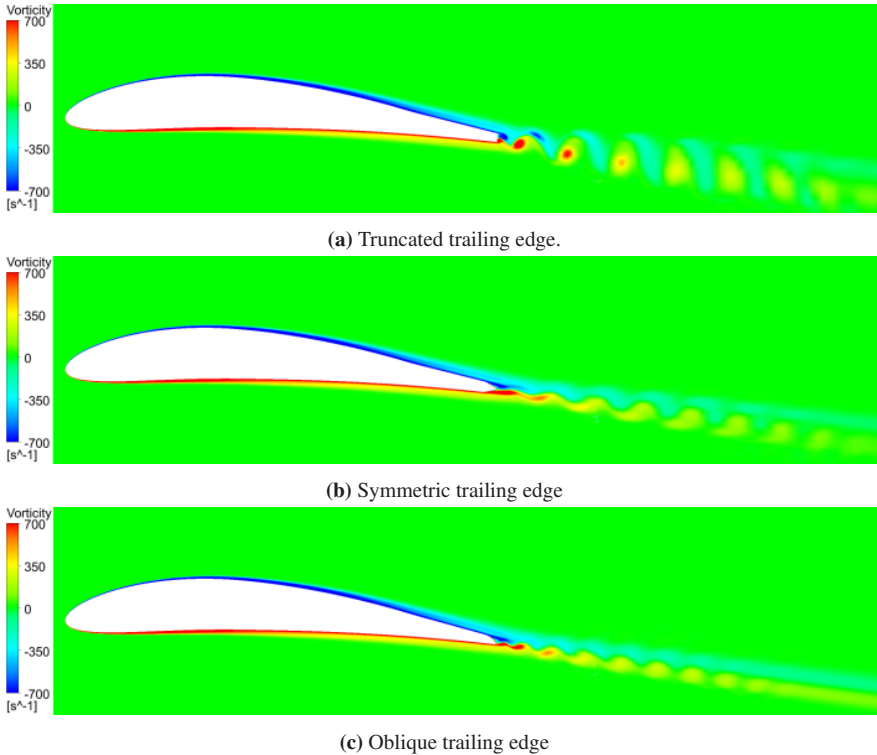


Figure 5.3: Instantaneous vorticity field at 50% span at $\alpha = 3^\circ$.

The structure of a turbine is sometimes exposed to premature cracking, particularly if one of the shedding frequencies overlap with one of the eigenmodes of the structure. In Figure 5.2, one can observe that the truncated and symmetric trailing edges exhibit multiple peaks of harmonic shedding frequencies compared to the oblique trailing edge, where one prominent frequency peak is shown. Making the oblique trailing edge shape suitable for turbine blades, as resonance is less likely to occur at higher frequencies.

The numerical simulation results obtained at $\alpha = 3^\circ$ are shown in Figure 5.3 and Figure 5.4. Figure 5.3 illustrates the streamwise vorticity field at mid-span for hydrofoils at $\alpha = 3^\circ$. By comparing Figure 5.1 and Figure 5.3, it is observed that wake width and wake structure decrease at $\alpha = 3^\circ$. For symmetric and oblique

trailing edge hydrofoils, vortices shed from the upper and lower surface are less coherent than those shed at $\alpha = 0^\circ$. Although, vortex structures are weaker, the longitudinal spacing is shorter for all three hydrofoils, implying an increase in the frequency of vortex shedding.

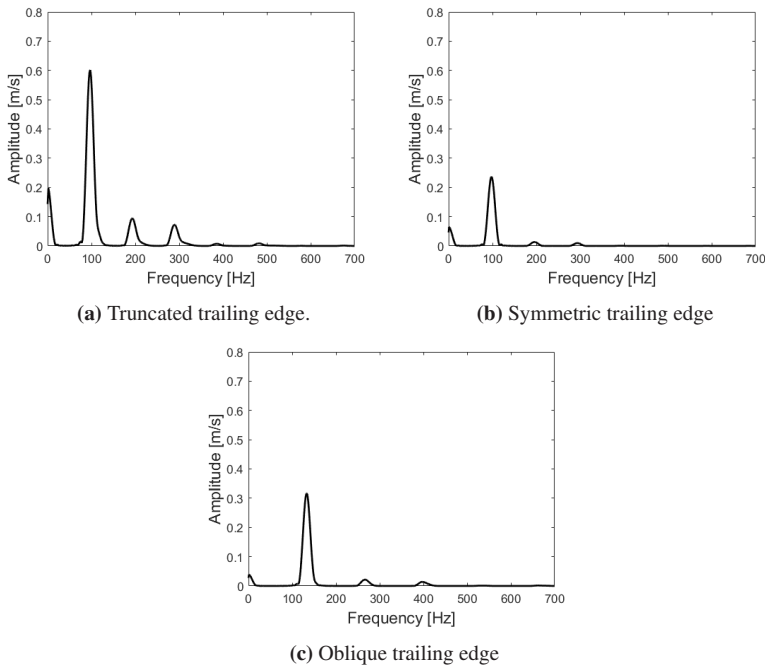


Figure 5.4: Amplitude frequency spectrum for hydrofoils at $\alpha = 3^\circ$.

In Figure 5.4 the amplitude frequency spectra is shown at $\alpha = 3^\circ$. The frequency for the truncated hydrofoil is 97 Hz, with an amplitude of 0.6 m/s. The frequency for the symmetric hydrofoil is 98 Hz, with an amplitude of 0.25 m/s. For the oblique trailing edge, the predicted frequency is 133 Hz, with an amplitude of 0.3 m/s. As observed from this figure, the influence of the trailing edge shape on the frequency is almost the same as at $\alpha = 0^\circ$, except for a relatively small increase of shedding frequencies. On the other hand, there is a notable reduction in their respective shedding strengths. Thus, additional harmonic modes that were observed in Figure 5.2 have dissipated and are barely visible in Figure 5.4. However, the oblique trailing edge's mitigating effect on vortex shedding is not as beneficial at $\alpha = 3^\circ$. The symmetric trailing edge yields a lower vortex strength, which may be reasoned by how the flow perceives the thickness of the trailing edge at a higher

angle of attack. As the lower surface of the symmetric trailing edge, allow fluid particles to travel to the sharp tip. Hence, the distance between shear layers is smaller and thereby cutting off the supply of circulation quicker. However, this needs to be further investigated. There is a possibility that the high Courant number spotted downstream of the trailing edges lead to inaccurate amplitude values.

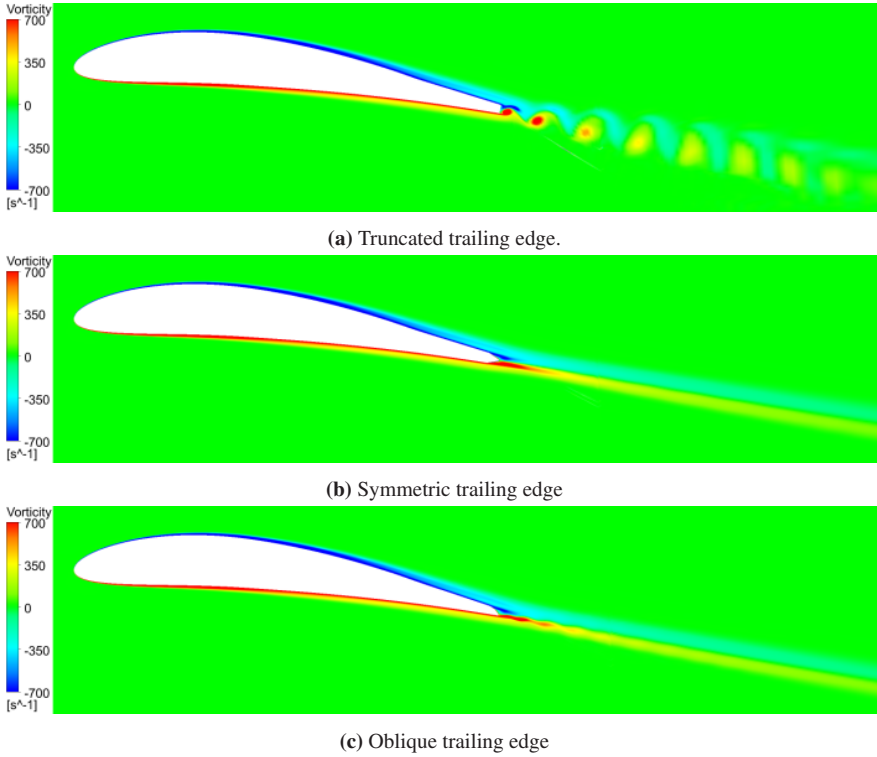


Figure 5.5: Instantaneous vorticity field at 50% span at $\alpha = 6^\circ$.

Angle of attack	Truncated	Symmetric	Oblique
0°	91 Hz	97 Hz	120 Hz
3°	97 Hz	98 Hz	133 Hz
6°	100 Hz	100 hz	146 Hz

Table 5.1: vortex shedding frequency at $\alpha = 0^\circ, 3^\circ$, and 6° .

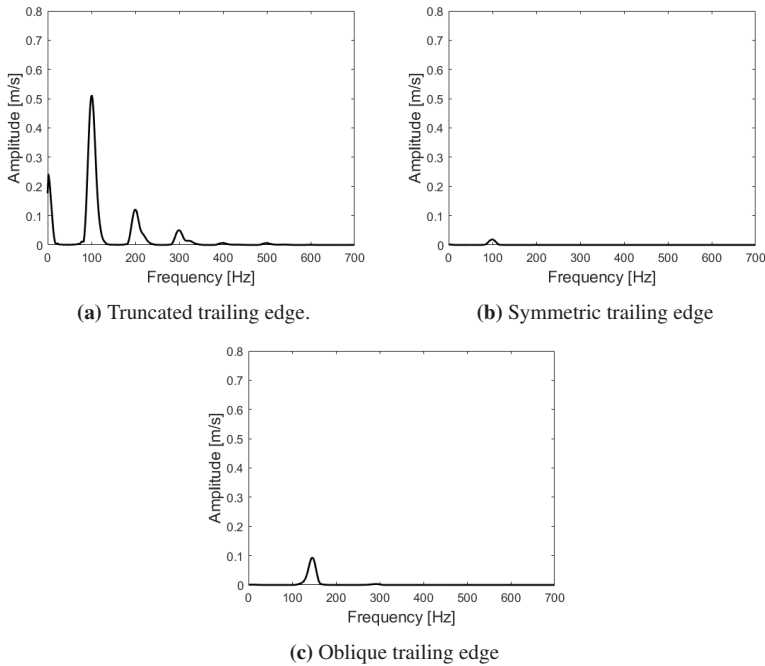


Figure 5.6: Amplitude frequency spectrum for hydrofoils at $\alpha = 6^\circ$.

The results obtained at $\alpha = 6^\circ$ are shown in Figure 5.5 and Figure 5.6. The instantaneous vorticity field at mid span with $\alpha = 6^\circ$, is depicted in Figure 5.5. When the angle of attack is increased to 6° , the vortex street in the wake of the hydrofoil with a symmetric trailing edge is no longer observed at mid span. While the vortex street in the wake of the hydrofoil with an oblique trailing edge is almost diminished. One would expect the formation of a vortex street to cease after a certain angle of attack due to boundary layer separation that usually occurs upstream on the suction side of the hydrofoil. In this case, however, there is no indication of early separation of the boundary layer. The reason for a weak vortex street is unclear, as it is developed at other locations along the span. This will be addressed later in this chapter.

In Figure 5.6, we see the amplitude frequency spectra for hydrofoils at $\alpha = 6^\circ$. The predicted frequency for the truncated trailing edge is 100 Hz, with an amplitude of 0.5 m/s. For the symmetric trailing edge, the frequency is 100 Hz, with an amplitude of 0.02 m/s. The predicted frequency for the oblique trailing edge is 146 Hz with an amplitude of 0.1 m/s. At $\alpha = 6^\circ$, the vortex shedding strength

is significantly reduced, except for the truncated trailing edge. Vortex shedding is non-existent for the symmetrical trailing edge shape. Nevertheless, there is a small velocity fluctuation in the same frequency as the truncated trailing edge. Indicating similarities at a higher angle of attack, but with different characteristics.

In Table 5.1, vortex shedding frequencies from every numerical simulation are presented. It is evident that the shedding frequencies obtained from the simulation are highly dependent on the trailing edge geometry. The frequency obtained at $\alpha = 0^\circ$ shows to be in good agreement with previous work, which suggests that the overall characteristic of vortex shedding is captured well.

As shown in Table 5.1, the shedding frequency directly depends on the angle of attack. The shedding frequency increases with the angle of attack. However, the change in shedding frequency for truncated and symmetric trailing edges is small compared to the oblique trailing edge, which also yields the highest frequency. Ausoni et al. [18] obtained experimental results showing that the shedding frequency followed the Strouhal relation for a truncated NACA 0009 hydrofoil. According to this, the increase in the shedding frequency in the present work suggests that the velocity around the hydrofoil increases. This may not be unreasonable to expect as a lift force is generated when the angle of attack increases. Thus, the pressure difference between the pressure and suction sides increases, which effectively increases the velocity, particularly on the suction side.

5.2 Interaction of hub vortex

In order to study the influence of hub vortex on trailing edge vortex, it is necessary to obtain an overview of how vortex shedding is distributed along the hydrofoil span. Figure 5.7, Figure 5.9, and Figure 5.11 show the cross-flow velocity component on cross-sectional planes placed parallel to the streamwise flow aligned with the lower surface of the trailing edges at $\alpha = 0^\circ$, 3° , and 6° , respectively.

In Figure 5.7, the oblique trailing edge clearly displays a difference in the vortex shedding pattern at $\alpha = 0^\circ$. For the truncated and symmetric trailing edges, vortices are shed at an angle relative to the hydrofoil span, while the oblique trailing edge shows curved vortex lines near the shroud. The curvature of vortex lines toward the shroud side is common for all three hydrofoils. This indicates that there is a common cause, which may be due to a thicker and evolved boundary layer at the shroud wall, which increases the flow velocity outside the shroud boundary layer to maintain mass conservation. If this is the case, then the vorticity lines are tilted as explained in section 3.1.

Figure 5.8 shows the streamwise component of vorticity on cross-sectional planes

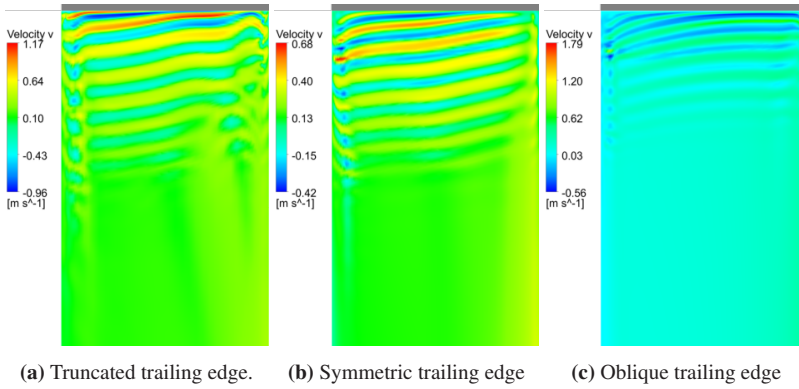


Figure 5.7: The cross flow velocity component is depicted for hydrofoils at $\alpha = 0^\circ$

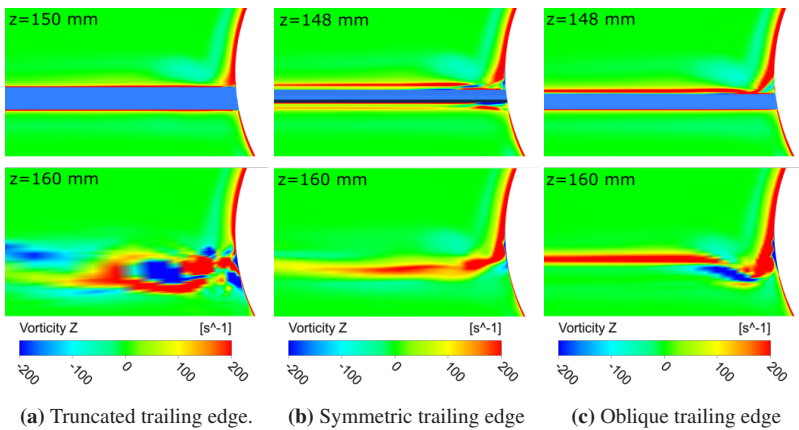


Figure 5.8: Streamwise vorticity is shown on planes perpendicular to mean flow for hydrofoils at $\alpha = 0^\circ$.

perpendicular to the mean flow. The planes are placed at two locations, denoted by the distance from the leading edge, z . The first plane for the truncated trailing edge is placed at the edge end, while for the symmetric and oblique trailing edge, its located further upstream on the trailing edge.

The hub vortex development is quite different for each trailing edge geometry, as seen in Figure 5.8. The corner vortex formed by the cross flow at the hub surface, evolve differently downstream of the trailing edges. For the truncated trailing edge, flow is significantly chaotic and exist of multiple vortexes. That is developed as

flow separates from the trailing edge. For the symmetric and oblique trailing edge, separation of flow is indicated to occur further upstream on the trailing edges. Consequently, the corner vortex is not attached at the junction between hub and blade surface. For these hydrofoils, the generated hub vortex is not as turbulent in comparison to the truncated one. Although, the truncated and symmetric trailing edges show similar vortex shedding pattern in Figure 5.7, there is a difference in the corner vortex. This might suggest that the vortex shedding occurring with an angle may not be caused by the hub vortex. Nevertheless, it has an effect on vortex shedding near the hub, where the structures are smeared together, in particular for the truncated trailing edge. The wake for the truncated one is distorted near the hub. This corresponds well with the more turbulent structures observed in Figure 5.8.

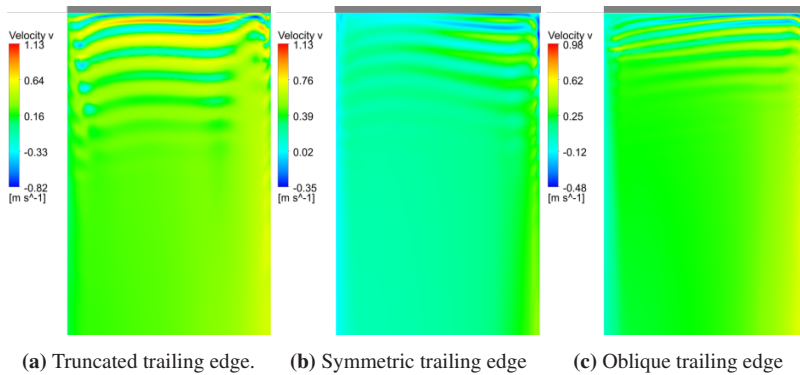


Figure 5.9: The cross flow velocity component is depicted for hydrofoils at $\alpha = 3^\circ$.

When angle of attack is increased to 3° , the angle of vortex shedding relative to the hydrofoil span is significantly decreased for truncated and symmetric trailing edges, as shown in Figure 5.9. The truncated trailing edge display almost parallel vortex shedding in the mid section of the span, but exhibit curvature near the hub and shroud. The reduced angle may be explained by a shift in the spanwise pressure gradient, which then even out the streamwise velocity along the span. The curvature near the span ends, is caused by the boundary conditions at both span ends, where vortex filaments seem to be induced. The symmetric also replicate the same pattern. On other hand, the vortex pattern remain the same for the oblique trailing edge, i.e. parallel vortex shedding still persist.

Figure 5.10 shows the stream wise vorticity field at $\alpha = 3^\circ$. From the figure, the the layer of vorticity along the hydrofoil span compared to Figure 5.8 is similar, and does not show any remarkabel difference compared to Figure 5.8. However, the hub vortex is increased, which is expected with a larger angle of attack.

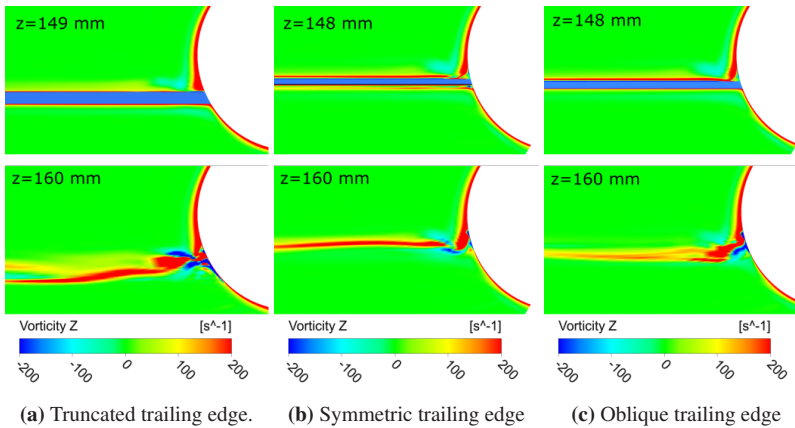


Figure 5.10: Streamwise vorticity is shown on planes perpendicular to mean flow for hydrofoils at $\alpha = 3^\circ$.

In Figure 5.11, the velocity component perpendicular to the flow is depicted for hydrofoils at $\alpha = 6^\circ$. From this figure, it is observed that the vortex street is diminished near the shroud side. The hydrofoil with the highest strength of vortex shedding, i.e. the truncated as previously illustrated in Figure 5.6, show the most visible vortex street.

Another interesting observation, is the influence from the hub vortex. At $\alpha = 6^\circ$, the swirl velocity generated from the hub vortex is in the range of 0.75 m/s, which is larger than those encounter at $\alpha = 0^\circ$ and 3° . The vortex shedding is more parallel and stronger near the hub side, indicating that the shedding frequency differs along the hydrofoil span. This may be due to the high swirl velocity, which may decrease the streamwise velocity. As velocity is a vector, which can change its magnitude and orientation. The orientation of the vector can be altered by the swirl velocity, reducing the streamwise component of the velocity vector. Thus, frequency of vortex shedding is lower, which in turn should increase the strength of vortices from trailing edges. If this is the case, it would be in line with the previous remark about the inverse correlation between frequency and vortex strength. Another case, could be that the frequency stays relatively similar along the span, but the strength increase due to the hub vortex. The hub vortex generate a high swirl velocity or cross flow velocity that is likely to contribute the velocity fluctuations near the hub.

Figure 5.12 depicts the streamwise vorticity field at $\alpha = 6^\circ$. The corner vortices that evolve downstream the trailing edge, is indicated to be more suppressed as a consequence of a stronger hub vortex at the trailing edge exit. The effect from

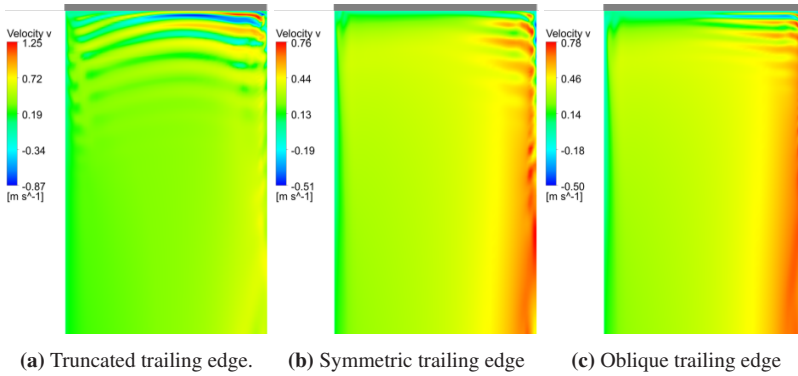


Figure 5.11: The cross flow velocity component is depicted for hydrofoils at $\alpha = 6^\circ$

the corner vortices that was observed for the truncated trailing edge at $\alpha = 0^\circ$ and 3° in Figure 5.7(a) and Figure 5.9(a), is no longer observed. Furthermore, when the hub vortex strength for each hydrofoil at $\alpha = 6^\circ$ is compared, results show that the oblique one has the strongest hub vortex. The symmetric has the second strongest hub vortex, while the weakest hub vortex generated is obtained from the truncated trailing edge. This difference can be traced back to the trailing edge shape, since the hydrofoils are based on the same NACA profile. However, surface gradient towards the trailing edge may play a role, as the last 10% of the chords were modified differently.

In Figure 5.13, the streamwise velocity field is projected on the suction side (SS) and pressure side (PS) of the blade surface at 0.5 mm offset from the blade surface. At the SS side of the blades, the magnitude of the streamwise velocity increases from the shroud side to the hub side, which indicates that the frequency changes along the span. Although, the strength of the trailing edge vortex increase near the hub, it is unclear whether the shedding frequency becomes higher or lower.

It is well known that the trailing edge shape affects the dynamic of vortex shedding. The numerical result also shows that the trailing edge shape affects the generated hub vortex. Depending on the trailing edge shape, different level of vortical structures was developed downstream of the trailing edges. Its influence along the span is not properly understood, apart from the effects near the hub. However, there is most likely a disturbance that translates along the span from the hub vortex. Thus, there may be a modulation in the spanwise direction that can be studied by comparing time steps. However, such a study was not performed.

The hub vortex interaction is more evident with higher angles of attack, as its

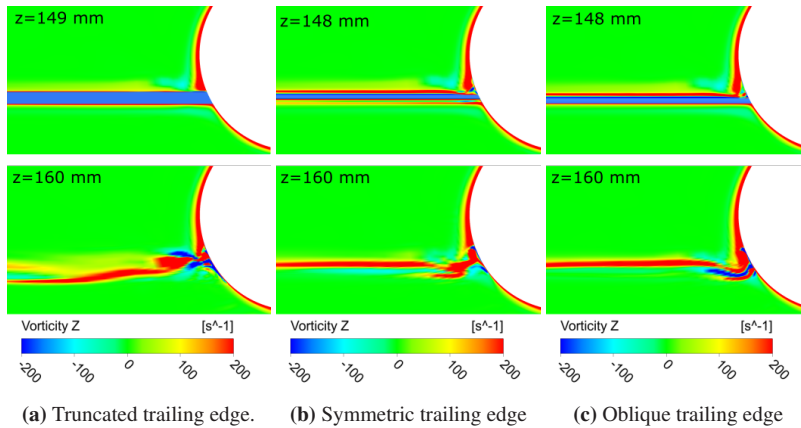


Figure 5.12: Streamwise vorticity is shown on planes perpendicular to mean flow for hydrofoils at $\alpha = 6^\circ$

strength also increase. Comparing vortex shedding lines at all angles of attack, it is observed that the vortex shedding become parallel and stronger near the hub. The result shows that the streamwise velocity along the hub is not constant. Thus, the increased velocity in combination with stronger swirl velocity results in stronger vortex shedding near the hub. This finding suggests that the hub vortex affect the shedding frequencies along the span, Which in turn can alter the fluid forces along the hydrofoil span. It is, however, unclear how the value of frequency changes. This can be further investigated by measuring different locations along the span.

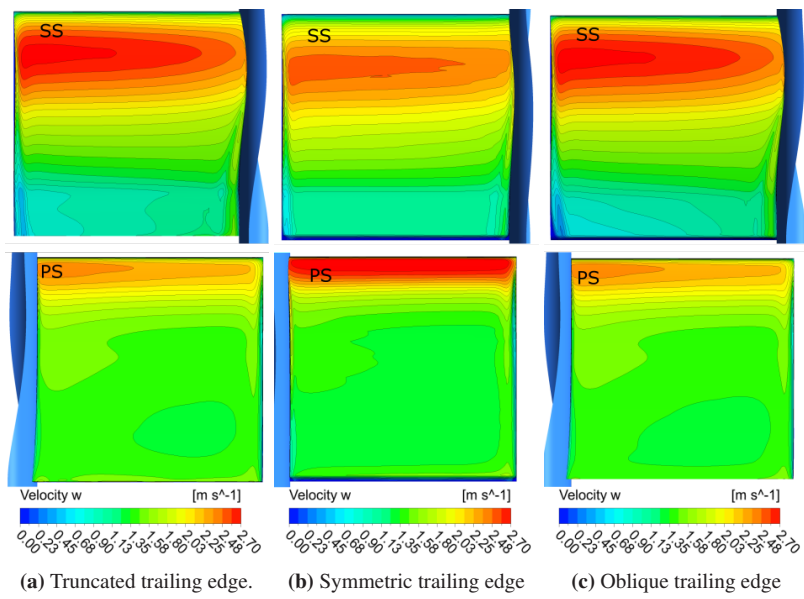


Figure 5.13: Streamwise velocity field on blade surface with 0.5 mm surface offset. $\alpha = 6^\circ$

Chapter 6

Conclusions

In this master thesis, CFD simulations were conducted on three-bladed circular cascades with the SAS-SST turbulence model. The main purpose of the simulations was to investigate the factors that affect vortex shedding and its interaction with the hub vortex. Simulations were therefore performed for a truncated, symmetric and oblique trailing edge shape at three angles of attack.

Firstly, it was found that vortex shedding depends on the trailing edge shape. The oblique trailing edge shape yielded the highest shedding frequency, while the symmetric one had the second-highest frequency and the truncated one had the lowest frequency. Secondly, the vortex shedding frequency could be increased by increasing the angle of attack. Furthermore, the overall trend suggests that shedding frequency is negatively correlated with the vortex strength.

Finally, it was found that the hub vortex is influenced by the trailing edge shape. The result indicates that the curvature of vortex shedding along the span arise from the hub vortex. However, this interaction is not properly understood. It was demonstrated that the strength of vortex shedding increased near the hub side when the angle of attack increased. This is thought to be a result of the increased hub vortex strength and the increase in streamwise velocity near the hub. This effect indicates that the shedding frequency differs along the span. From a structural point of view, this effect is important, since it implies that the hub vortex can alter the fluctuating forces along the span.

The numerical results in this study have contributed to shedding light upon vortex interaction that can occur in hydraulic turbines, and facilitate further studies on the phenomenon.

Chapter 7

Future work

For further work, one should find a better mesh topology around the hydrofoil. This would increase the solution accuracy especially in the wake of the hydrofoil. As the mesh topology used in this study had a region with Courant numbers above one. The inaccuracy of the existing mesh can also be further inspected and addressed.

The angle of attack studied in the present work, show that the change in vortex shedding is small with a higher angle of attack. Therefore, it would be interesting to investigate the dynamic of vortex shedding beyond the angle of attack of 6° .

It would be interesting to investigate the frequency of vortex shedding along with the hub by placing multiple monitor points along the span. By doing so, the influence from the hub vortex can be further inspected.

As the vortex interaction is a complex phenomenon to break down, it would help to study this phenomenon by comparing several time steps, as this is a turbulent phenomenon that is most likely a function of time and space.

For future work, the Reynolds number used for simulation can be increased. This would potentially replicate the flow regime in hydraulic turbines. Thus, the result from the numerical simulation is more transferable to industrial applications.

References

- [1] Dyke, M. V., 1982, *An Album of Fluid Motion*, 14th ed., Parabolic Press, Inc., Stanford, Calif.
- [2] Heskestad, G. and Olberts, D. R., 1960, "Influence of Trailing-Edge Geometry on Hydraulic-Turbine-Blade Vibration Resulting From Vortex Excitation," *Journal of Engineering for Power*, **82**(2), pp. 103–109.
- [3] Zobeiri, A., Ausoni, P., Avellan, F., and Farhat, M., 2012, "How oblique trailing edge of a hydrofoil reduces the vortex-induced vibration," *Journal of Fluids and Structures*, **32**, pp. 78–89.
- [4] Greitzer, E. M., Tan, C. S., and Graf, M. B., 2007, *Internal Flow: Concepts and Applications*, illustrated edition ed., Cambridge University Press.
- [5] "13.42 Lecture: Vortex Induced Vibrations Prof. A. H. Techet 21 April 2005," accessed 2021-05-23, <https://studylib.net/doc/13608920/13.42-lecture--vortex-induced-vibrations-prof.-a.-h.-tech>.
..
- [6] Brekke, H., 1994, "A review on oscillatory problems in Francis turbines and simulation of unsteady flow in conduit systems," Proceedings of the 17th IAHR Symposium, Beijing, China, pp. 15–19.
- [7] Egorov, Y. and Menter, F., 2008, "Development and Application of SST-SAS Turbulence Model in the DESIDER Project," *Advances in Hybrid RANS-LES Modelling*, S.-H. Peng and W. Haase, eds., Notes on Numerical Fluid Mechanics and Multidisciplinary Design, Springer, Berlin, Heidelberg, pp. 261–270, doi:10.1007/978-3-540-77815-8_27.
- [8] Secretariat, R., "Renewables Global Status Report," accessed 2021-06-08, <https://www.ren21.net/reports/global-status-report/>

- [9] Siemonsmeier, M., Baumanns, P., van Bracht, N., Schönefeld, M., Schönbauer, A., Moser, A., Dahlhaug, O. G., and Heidenreich, S., 2018, “Hydropower Providing Flexibility for a Renewable Energy System: Three European Energy Scenarios,” Report, HydroFlex, Accepted: 2019-01-08T10:05:06Z, accessed 2021-06-06, <https://ntnuopen.ntnu.no/ntnu-xmlui/handle/11250/2579612>
- [10] Trivedi, C., Gandhi, B., and Michel, C. J., 2013, “Effect of transients on Francis turbine runner life: a review,” *Journal of Hydraulic Research*, **51**(2), pp. 121–132.
- [11] Sick, M., Michler, W., Weiss, T., and Keck, H., 2009, “Recent developments in the dynamic analysis of water turbines,” *Proceedings of the Institution of Mechanical Engineers, Part A: Journal of Power and Energy*, **223**(4), pp. 415–427.
- [12] Bergan, C. W., 2019, *Dynamic Loads on Francis Turbines: An Experimental Study*, NTNU, Accepted: 2019-05-06T12:19:18Z ISSN: 1503-8181.
- [13] Griffin, O. M., 1995, “A note on bluff body vortex formation,” *Journal of Fluid Mechanics*, **284**, pp. 217–224, Publisher: Cambridge University Press.
- [14] Williamson, C. H. K. and Roshko, A., 1988, “Vortex formation in the wake of an oscillating cylinder,” *Journal of Fluids and Structures*, **2**(4), pp. 355–381.
- [15] Kamalaraja, A., 2020, “CFD study of radial cascade,” Msc, project, Norwegian University of Science and Technology (NTNU), Trondheim, Norway., Department of Energy and Process Engineering.
- [16] Strouhal, V., 1878, “Ueber eine besondere Art der Tonerregung,” *Annalen der Physik*, **241**(10), pp. 216–251.
- [17] Navrose and Mittal, S., 2016, “Lock-in in vortex-induced vibration,” *Journal of Fluid Mechanics*, **794**, pp. 565–594, Publisher: Cambridge University Press.
- [18] Ausoni, P., Farhat, M., Escaler, X., Egusquiza, E., and Avellan, F., 2007, “Cavitation Influence on von Kármán Vortex Shedding and Induced Hydrofoil Vibrations,” *Journal of Fluids Engineering*, **129**(8), pp. 966–973.
- [19] Hu, J., Wang, Z., Zhao, W., Sun, S., Sun, C., and Guo, C., 2020, “Numerical Simulation on Vortex Shedding from a Hydrofoil in Steady Flow,” *Journal of Marine Science and Engineering*, **8**(3), p. 195.

-
- [20] Ausoni, P., Zobeiri, A., Avellan, F., and Farhat, M., 2012, “The Effects of a Tripped Turbulent Boundary Layer on Vortex Shedding from a Blunt Trailing Edge Hydrofoil,” *Journal of Fluids Engineering*, **134**(051207).
- [21] Lockey, K. J., Keller, M., Sick, M., Staehle, M., and Gehrler, A., 2006, “Flow induced vibrations at stay vanes: Experience at site and CFD simulation of von Kármán vortex shedding,” .
- [22] Cengel, Y. and Cimbala, J., 2013, *Fluid Mechanics Fundamentals and Applications*, 3rd ed., McGraw-Hill Education, New York.
- [23] Langston, L., 2001, “Secondary Flows in Axial Turbines—A Review,” *Annals of the New York Academy of Sciences*, **934**, pp. 11–26.
- [24] ILIEVA, G., 2017, “A Deep Insight to Secondary Flows,” *Defect and Diffusion Forum*, **379**, pp. 83–107.
- [25] Gongwer, C. A., 1952, “A Study of Vanes Singing in Water,” *Journal of Applied Mechanics*, **19**(4), pp. 432–438.
- [26] Donaldson, R., 1956, “Hydraulic turbine runner vibration,” *Journal of Engineering for Power*, **78**, pp. 1141–1147.
- [27] Versteeg, H. and Malalasekera, W., 2007, *An Introduction to Computational Fluid Dynamics: The Finite Volume Method*, 2nd ed., Pearson, Harlow, England ; New York.
- [28] Ferziger, J. H. and Peric, M., 2001, *Computational Methods for Fluid Dynamics*, 3rd ed., Springer, Berlin ; New York.
- [29] Menter, F. R. and Egorov, Y., 2006, “SAS turbulence modelling of technical flows,” *Direct and Large-Eddy Simulation VI*, Springer, pp. 687–694.
- [30] “NACA 6412 (naca6412-il),” accessed 2021-06-10, <http://airfoiltools.com/airfoil/details?airfoil=naca6412-il>
- [31] “ANSYS Help, TurboSystem User’s guide 2019, ANSYS Inc., Canonsburg, Pennsylvania, USA.” .
- [32] Vu, T., Nennemann, B., Ausoni, P., Farhat, M., and Avellan, F., 2007, “Unsteady CFD Prediction of von Kármán Vortex Shedding in Hydraulic Turbine Stay Vanes,” *Infoscience*, Conference Name: Hydro 2007 Number: CONF.
- [33] “ANSYS Help, CFX -Solver Modelling Guide 2019, ANSYS Inc., Canonsburg, Pennsylvania, USA.” .

- [34] 2008, "Procedure for Estimation and Reporting of Uncertainty Due to Discretization in CFD Applications," *Journal of Fluids Engineering*, **130**(078001).

Appendices

Appendix A

A.1 Geometry coordinates

Hub coordinates:

data.txt

```

2.500000000e-02  0.000000000e+00  -0.50000
2.500000000e-02  0.000000000e+00  -1.666666667e-01
2.500000000e-02  0.000000000e+00  -1.333333333e-01
2.500000000e-02  0.000000000e+00  -1.000000000e-01
2.500000000e-02  0.000000000e+00  -6.666666667e-02
2.500000000e-02  0.000000000e+00  -3.333333333e-02
2.500000000e-02  0.000000000e+00   0.000000000e+00
2.500000000e-02  0.000000000e+00   3.333333333e-02
2.500000000e-02  0.000000000e+00   6.666666667e-02
2.500000000e-02  0.000000000e+00   1.000000000e-01
2.500000000e-02  0.000000000e+00   1.333333333e-01
2.500000000e-02  0.000000000e+00   1.666666667e-01
2.500000000e-02  0.000000000e+00   2.000000000e-01
2.500000000e-02  0.000000000e+00   2.333333333e-01
2.500000000e-02  0.000000000e+00   2.666666667e-01
2.500000000e-02  0.000000000e+00   3.000000000e-01
2.500000000e-02  0.000000000e+00   3.333333333e-01
2.500000000e-02  0.000000000e+00   3.666666667e-01
2.500000000e-02  0.000000000e+00   4.000000000e-01
2.500000000e-02  0.000000000e+00   4.333333333e-01
2.500000000e-02  0.000000000e+00   4.666666667e-01
2.500000000e-02  0.000000000e+00   5.000000000e-01
2.500000000e-02  0.000000000e+00   5.333333333e-01
2.500000000e-02  0.000000000e+00   5.666666667e-01
2.500000000e-02  0.000000000e+00   6.000000000e-01
2.500000000e-02  0.000000000e+00   6.333333333e-01
2.500000000e-02  0.000000000e+00   6.666666667e-01

```

2.500000000e-02	0.000000000e+00	7.000000000e-01
2.500000000e-02	0.000000000e+00	7.333333333e-01
2.500000000e-02	0.000000000e+00	7.666666667e-01
2.500000000e-02	0.000000000e+00	1.00000

Shroud coordinates:

data.txt

1.750000000e-01	0.000000000e+00	-0.50000
1.750000000e-01	0.000000000e+00	-1.666666667e-01
1.750000000e-01	0.000000000e+00	-1.333333333e-01
1.750000000e-01	0.000000000e+00	-1.000000000e-01
1.750000000e-01	0.000000000e+00	-6.666666667e-02
1.750000000e-01	0.000000000e+00	-3.333333333e-02
1.750000000e-01	0.000000000e+00	0.000000000e+00
1.750000000e-01	0.000000000e+00	3.333333333e-02
1.750000000e-01	0.000000000e+00	6.666666667e-02
1.750000000e-01	0.000000000e+00	1.000000000e-01
1.750000000e-01	0.000000000e+00	1.333333333e-01
1.750000000e-01	0.000000000e+00	1.666666667e-01
1.750000000e-01	0.000000000e+00	2.000000000e-01
1.750000000e-01	0.000000000e+00	2.333333333e-01
1.750000000e-01	0.000000000e+00	2.666666667e-01
1.750000000e-01	0.000000000e+00	3.000000000e-01
1.750000000e-01	0.000000000e+00	3.333333333e-01
1.750000000e-01	0.000000000e+00	3.666666667e-01
1.750000000e-01	0.000000000e+00	4.000000000e-01
1.750000000e-01	0.000000000e+00	4.333333333e-01
1.750000000e-01	0.000000000e+00	4.666666667e-01
1.750000000e-01	0.000000000e+00	5.000000000e-01
1.750000000e-01	0.000000000e+00	5.333333333e-01
1.750000000e-01	0.000000000e+00	5.666666667e-01
1.750000000e-01	0.000000000e+00	6.000000000e-01
1.750000000e-01	0.000000000e+00	6.333333333e-01
1.750000000e-01	0.000000000e+00	6.666666667e-01
1.750000000e-01	0.000000000e+00	7.000000000e-01
1.750000000e-01	0.000000000e+00	7.333333333e-01
1.750000000e-01	0.000000000e+00	7.666666667e-01
1.750000000e-01	0.000000000e+00	1.00000

Truncated trailing edge coordinates:

data.txt

Symmetric trailing edge coordinates:

data.txt

```
# Profile 1 at      0.5000%
2.546665541e-02 -3.809456950e-03 1.459980194e-01
2.550809645e-02 -3.521294600e-03 1.465067088e-01
2.557278284e-02 -3.015837799e-03 1.473989854e-01
2.562736361e-02 -2.510126371e-03 1.482917115e-01
2.570639342e-02 -1.497944302e-03 1.500785039e-01
2.573541641e-02 -8.665116160e-04 1.477968871e-01
2.574892727e-02 -2.350417631e-04 1.455151360e-01
2.574687691e-02 -4.010352724e-04 1.423477912e-01
2.574375611e-02 -5.670287361e-04 1.391804472e-01
2.574026907e-02 -7.078475191e-04 1.360118039e-01
2.573412962e-02 -9.039208418e-04 1.310556169e-01
2.572694669e-02 -1.089364041e-03 1.254208898e-01
2.572041133e-02 -1.234074918e-03 1.197847610e-01
2.571289030e-02 -1.381945194e-03 1.104738109e-01
2.571134854e-02 -1.410339038e-03 9.936134124e-02
2.571589694e-02 -1.324818743e-03 9.063915101e-02
2.572762851e-02 -1.073140849e-03 7.877730441e-02
2.574079281e-02 -6.885386221e-04 6.662219167e-02
2.574815228e-02 -3.084709627e-04 5.683885620e-02
2.574967962e-02 1.284492941e-04 4.930611112e-02
2.573584287e-02 8.537515594e-04 3.987430584e-02
2.571455312e-02 1.350650915e-03 3.421897179e-02
2.568257523e-02 1.862210960e-03 2.856456738e-02
2.565253682e-02 2.238270505e-03 2.426529952e-02
2.563653811e-02 2.414624985e-03 2.211494253e-02
2.562060254e-02 2.578221342e-03 1.996379335e-02
2.560743701e-02 2.705858450e-03 1.810095174e-02
2.559250331e-02 2.843637537e-03 1.571637895e-02
2.558131348e-02 2.942600967e-03 1.333158094e-02
2.557678932e-02 2.981668657e-03 1.159242276e-02
2.557660094e-02 2.983284150e-03 9.853046840e-03
2.558033922e-02 2.951058337e-03 8.504708872e-03
2.558838331e-02 2.880475568e-03 7.156147987e-03
2.559821149e-02 2.791785900e-03 6.110713715e-03
2.561184372e-02 2.663824530e-03 5.065051564e-03
2.562718230e-02 2.511976763e-03 4.163247025e-03
2.564186073e-02 2.357430406e-03 3.457926472e-03
2.565892778e-02 2.163775627e-03 2.763197277e-03
2.567327351e-02 1.986335177e-03 2.253689078e-03
2.568896508e-02 1.771884082e-03 1.754182812e-03
```

2.570416438e-02	1.535719213e-03	1.314027903e-03
2.571622967e-02	1.318344322e-03	9.875342120e-04
2.572215350e-02	1.197213165e-03	8.324840483e-04
2.572790628e-02	1.066460704e-03	6.837682838e-04
2.573078050e-02	9.947034033e-04	6.096406011e-04
2.573499461e-02	8.789496756e-04	5.003554048e-04
2.573886104e-02	7.573191033e-04	3.982656350e-04
2.574524608e-02	4.947771695e-04	2.176851889e-04
2.574768947e-02	3.449451798e-04	1.362162278e-04
2.574990551e-02	6.975755146e-05	2.221515950e-05
2.574906101e-02	-2.199027462e-04	-5.371843495e-05
2.574724381e-02	-3.767442026e-04	-7.772128541e-05
2.574104552e-02	-6.790253461e-04	-9.239188200e-05
2.573126983e-02	-9.819638802e-04	-6.827523415e-05
2.571605225e-02	-1.321800630e-03	1.491597897e-06
2.569722294e-02	-1.647796385e-03	1.076403476e-04
2.567376183e-02	-1.980013569e-03	2.523812648e-04
2.564694479e-02	-2.301461004e-03	4.253379334e-04
2.561694321e-02	-2.614329892e-03	6.229417220e-04
2.557152844e-02	-3.026455537e-03	9.246228122e-04
2.552208263e-02	-3.418449717e-03	1.252868824e-03
2.548417832e-02	-3.690413959e-03	1.503149160e-03
2.540985831e-02	-4.171522562e-03	1.988953242e-03
2.533095278e-02	-4.626589591e-03	2.497079156e-03
2.524228093e-02	-5.088197485e-03	3.059147199e-03
2.514936382e-02	-5.529195196e-03	3.638785249e-03
2.502128953e-02	-6.082562823e-03	4.423642159e-03
2.487574017e-02	-6.652822802e-03	5.298733928e-03
2.472461214e-02	-7.194168077e-03	6.191754877e-03
2.459432753e-02	-7.627683360e-03	6.950775398e-03
2.439548590e-02	-8.241527036e-03	8.093638338e-03
2.419148887e-02	-8.822378728e-03	9.251047978e-03
2.397442945e-02	-9.396235018e-03	1.047005474e-02
2.375356142e-02	-9.941369126e-03	1.170184621e-02
2.352152109e-02	-1.047857555e-02	1.299024405e-02
2.328712373e-02	-1.098964823e-02	1.429047115e-02
2.302403004e-02	-1.153067823e-02	1.575213952e-02
2.276093452e-02	-1.204169257e-02	1.722192167e-02
2.245739151e-02	-1.259873273e-02	1.893463830e-02
2.215667348e-02	-1.312037805e-02	2.065738870e-02
2.155782556e-02	-1.408270773e-02	2.420210536e-02
2.097952658e-02	-1.493057148e-02	2.784722632e-02
2.070196890e-02	-1.531309844e-02	2.971124345e-02
2.043697506e-02	-1.566501039e-02	3.158560712e-02
2.029856144e-02	-1.584395480e-02	3.261100675e-02
2.003842176e-02	-1.617170843e-02	3.464697858e-02
1.979830878e-02	-1.646479485e-02	3.668848284e-02
1.938509016e-02	-1.694935926e-02	4.077928983e-02
1.906995586e-02	-1.730315820e-02	4.487910531e-02
1.895160293e-02	-1.743270623e-02	4.693109353e-02
1.890252464e-02	-1.748591040e-02	4.795924338e-02

```
1.886025804e-02 -1.753149072e-02 4.898882802e-02
1.882809142e-02 -1.756603181e-02 4.991567717e-02
1.879900208e-02 -1.759715945e-02 5.094201323e-02
1.877681739e-02 -1.762082940e-02 5.196796944e-02
1.875319492e-02 -1.764596782e-02 5.401874624e-02
1.878759373e-02 -1.760933905e-02 5.813304445e-02
1.892505530e-02 -1.746152289e-02 6.227751683e-02
1.913427152e-02 -1.723200956e-02 6.652570736e-02
1.940809033e-02 -1.692301775e-02 7.089304347e-02
1.985739406e-02 -1.639348655e-02 7.678455114e-02
2.040348243e-02 -1.570860926e-02 8.292652381e-02
2.101599607e-02 -1.487919384e-02 8.916226622e-02
2.167411290e-02 -1.390306908e-02 9.549133937e-02
2.201522380e-02 -1.335636257e-02 9.870624852e-02
2.239121605e-02 -1.271597200e-02 1.022419801e-01
2.276383830e-02 -1.203620229e-02 1.057700051e-01
2.348554637e-02 -1.055895883e-02 1.128084161e-01
2.414673387e-02 -8.944145754e-03 1.197493196e-01
2.459451936e-02 -7.627064810e-03 1.264822812e-01
2.486898092e-02 -6.678045232e-03 1.313337008e-01
2.510468030e-02 -5.728658418e-03 1.361869977e-01
2.529382241e-02 -4.825458328e-03 1.408041866e-01
2.537583308e-02 -4.373739284e-03 1.431133894e-01
2.541373325e-02 -4.147850344e-03 1.442681412e-01
2.544957508e-02 -3.921941902e-03 1.454229926e-01

# Profile 2 at 99.5000%
1.742083538e-01 -3.809456950e-03 1.459980194e-01
1.742297916e-01 -2.653714814e-03 1.480382366e-01
1.742435613e-01 -1.497944302e-03 1.500785039e-01
1.742478456e-01 -8.664934374e-04 1.477968214e-01
1.742498415e-01 -2.350417631e-04 1.455151360e-01
1.742495385e-01 -4.010352501e-04 1.423477916e-01
1.742490774e-01 -5.670287361e-04 1.391804472e-01
1.742485623e-01 -7.078474816e-04 1.360118047e-01
1.742476718e-01 -9.007693974e-04 1.311417225e-01
1.742466104e-01 -1.086864334e-03 1.255059311e-01
1.742456431e-01 -1.232221318e-03 1.198687364e-01
1.742446864e-01 -1.360797215e-03 1.123942908e-01
1.742442409e-01 -1.416694067e-03 1.012860675e-01
1.742444923e-01 -1.385420767e-03 9.569561026e-02
1.742450251e-01 -1.316707611e-03 9.010504671e-02
1.742455289e-01 -1.248265598e-03 8.623382062e-02
1.742465038e-01 -1.103813400e-03 7.993496856e-02
1.742475537e-01 -9.233273688e-04 7.363715776e-02
1.742485978e-01 -6.990562757e-04 6.691912366e-02
1.742494122e-01 -4.526059344e-04 6.020173044e-02
1.742498663e-01 -2.158492895e-04 5.500540229e-02
1.742497930e-01 2.686047809e-04 4.729424208e-02
1.742476680e-01 9.014884120e-04 3.931405380e-02
1.742421806e-01 1.650754826e-03 3.090519308e-02
```

1.742378064e-01	2.061384395e-03	2.632143674e-02
1.742328522e-01	2.444527054e-03	2.173564399e-02
1.742296255e-01	2.664599802e-03	1.872780294e-02
1.742267958e-01	2.843610254e-03	1.571691907e-02
1.742255170e-01	2.920910747e-03	1.396365341e-02
1.742246606e-01	2.971554374e-03	1.221104884e-02
1.742243839e-01	2.987735439e-03	1.050121614e-02
1.742248433e-01	2.960825998e-03	8.792452104e-03
1.742257556e-01	2.906646515e-03	7.566877407e-03
1.742272695e-01	2.814441237e-03	6.342245747e-03
1.742289436e-01	2.708819890e-03	5.392636467e-03
1.742299693e-01	2.642023953e-03	4.918178648e-03
1.742305335e-01	2.604555011e-03	4.681050693e-03
1.742311334e-01	2.564111643e-03	4.443996499e-03
1.742317394e-01	2.522597291e-03	4.218374760e-03
1.742327433e-01	2.452276380e-03	3.870759046e-03
1.742338290e-01	2.373886561e-03	3.525532357e-03
1.742362535e-01	2.188709483e-03	2.843486708e-03
1.742385569e-01	1.996942747e-03	2.281411001e-03
1.742410978e-01	1.761342834e-03	1.732312570e-03
1.742429434e-01	1.568171287e-03	1.368782516e-03
1.742448137e-01	1.344400012e-03	1.023245728e-03
1.742461088e-01	1.164499546e-03	7.935422088e-04
1.742475031e-01	9.328196962e-04	5.496847650e-04
1.742481337e-01	8.064668017e-04	4.380095416e-04
1.742487034e-01	6.721961522e-04	3.340565940e-04
1.742491400e-01	5.474428736e-04	2.498867112e-04
1.742497694e-01	2.835012541e-04	1.069362862e-04
1.742500000e-01	1.432079710e-06	4.302076498e-07
1.742499392e-01	-1.456169749e-04	-3.825840276e-05
1.742494415e-01	-4.411899942e-04	-8.426190577e-05
1.742484218e-01	-7.416280181e-04	-9.050121648e-05
1.742457735e-01	-1.213635716e-03	-2.539286396e-05
1.742432182e-01	-1.537341758e-03	6.755635477e-05
1.742401491e-01	-1.852820676e-03	1.927639346e-04
1.742376810e-01	-2.071958420e-03	2.986419485e-04
1.742326509e-01	-2.458833270e-03	5.212193523e-04
1.742270507e-01	-2.827949009e-03	7.735986028e-04
1.742218187e-01	-3.133748240e-03	1.010571625e-03
1.742132078e-01	-3.580606648e-03	1.399928928e-03
1.742040422e-01	-4.001770147e-03	1.811380746e-03
1.741936508e-01	-4.431085287e-03	2.273101199e-03
1.741827529e-01	-4.840568386e-03	2.751873007e-03
1.741706621e-01	-5.257659173e-03	3.277021617e-03
1.741581054e-01	-5.658341642e-03	3.816276832e-03
1.741443832e-01	-6.065996167e-03	4.399226341e-03
1.741302339e-01	-6.459423342e-03	4.994406897e-03
1.741115186e-01	-6.945617069e-03	5.774217113e-03
1.740864474e-01	-7.547934485e-03	6.808197884e-03
1.740607853e-01	-8.118220525e-03	7.857528259e-03
1.740334421e-01	-8.684671813e-03	8.969855592e-03

```

1.740057071e-01 -9.223686716e-03 1.009533338e-02
1.739765843e-01 -9.757592834e-03 1.127834072e-02
1.739472754e-01 -1.026683448e-02 1.247317398e-02
1.739168747e-01 -1.076954926e-02 1.372128936e-02
1.738865041e-01 -1.124927576e-02 1.498043192e-02
1.738661333e-01 -1.155985218e-02 1.583362536e-02
1.738260420e-01 -1.214782403e-02 1.753893094e-02
1.737867470e-01 -1.269760102e-02 1.925183455e-02
1.737095472e-01 -1.371334043e-02 2.277826799e-02
1.736363511e-01 -1.461095778e-02 2.640297992e-02
1.735688419e-01 -1.539219366e-02 3.011785887e-02
1.735084837e-01 -1.605828748e-02 3.391669314e-02
1.734566259e-01 -1.660907668e-02 3.779406551e-02
1.734143941e-01 -1.704436652e-02 4.174542944e-02
1.733971671e-01 -1.721873777e-02 4.375310007e-02
1.733896151e-01 -1.729461959e-02 4.475919754e-02
1.733827771e-01 -1.736303851e-02 4.576678873e-02
1.733774448e-01 -1.741620369e-02 4.663954326e-02
1.733711298e-01 -1.747895428e-02 4.781585532e-02
1.733658122e-01 -1.753161915e-02 4.899199451e-02
1.733581409e-01 -1.760731328e-02 5.134376487e-02
1.733546224e-01 -1.764192112e-02 5.607966705e-02
1.733667308e-01 -1.752253250e-02 6.084421421e-02
1.733908491e-01 -1.728224364e-02 6.569848484e-02
1.734245936e-01 -1.694027289e-02 7.067357367e-02
1.734633634e-01 -1.653856327e-02 7.530378013e-02
1.735299044e-01 -1.582513152e-02 8.196064954e-02
1.736073056e-01 -1.495212119e-02 8.865125771e-02
1.736493263e-01 -1.445593221e-02 9.201454965e-02
1.736929088e-01 -1.392249727e-02 9.537327396e-02
1.737357430e-01 -1.337737226e-02 9.858627896e-02
1.737837551e-01 -1.273848333e-02 1.021214326e-01
1.738321376e-01 -1.206028351e-02 1.056485528e-01
1.739283865e-01 -1.058200733e-02 1.127042075e-01
1.740202998e-01 -8.944145754e-03 1.197493196e-01
1.740815308e-01 -7.660492744e-03 1.263113964e-01
1.741332782e-01 -6.376826933e-03 1.328735387e-01
1.741688230e-01 -5.318232139e-03 1.382851105e-01
1.741841802e-01 -4.788931482e-03 1.409909131e-01
1.741979278e-01 -4.259628653e-03 1.436967267e-01

```

Oblique trailing edge coordinates:

data.txt

```

# Profile 1 at      0.5000%
2.549580961e-02  3.609181674e-03  1.487477016e-01

```

2.543312464e-02	4.027241104e-03	1.491241240e-01
2.539746700e-02	4.246312504e-03	1.493213767e-01
2.536350129e-02	4.444693743e-03	1.495000000e-01
2.531566887e-02	4.709502083e-03	1.495000000e-01
2.526507178e-02	4.973796110e-03	1.495000000e-01
2.526784006e-02	4.959713580e-03	1.492312893e-01
2.527097938e-02	4.943693049e-03	1.489255994e-01
2.527410817e-02	4.927672513e-03	1.486199093e-01
2.528033411e-02	4.895631425e-03	1.480085290e-01
2.529265966e-02	4.831549185e-03	1.467857670e-01
2.531680617e-02	4.703384447e-03	1.443402381e-01
2.534155183e-02	4.568178045e-03	1.417603463e-01
2.536555274e-02	4.432971259e-03	1.391804471e-01
2.541440962e-02	4.143704114e-03	1.323300129e-01
2.546854507e-02	3.796802836e-03	1.211328904e-01
2.549292105e-02	3.629528413e-03	1.115715399e-01
2.549918430e-02	3.585261483e-03	1.005208413e-01
2.548806721e-02	3.663458707e-03	9.145005648e-02
2.545279906e-02	3.900964013e-03	7.975168411e-02
2.536826991e-02	4.417395387e-03	6.368818435e-02
2.530324523e-02	4.775801593e-03	5.516368121e-02
2.520632360e-02	5.263435237e-03	4.736625393e-02
2.512832151e-02	5.624051758e-03	4.264768680e-02
2.503618325e-02	6.020965719e-03	3.793110052e-02
2.493242187e-02	6.437145308e-03	3.326072702e-02
2.479896848e-02	6.933517320e-03	2.776773528e-02
2.466317345e-02	7.402052105e-03	2.227292418e-02
2.459537794e-02	7.624295646e-03	1.931577986e-02
2.453704487e-02	7.809989047e-03	1.635600970e-02
2.450489421e-02	7.910288224e-03	1.424097110e-02
2.448447709e-02	7.973260422e-03	1.212321172e-02
2.447975002e-02	7.987761832e-03	1.051548787e-02
2.448182061e-02	7.981413381e-03	9.710631691e-03
2.448742795e-02	7.964193128e-03	8.904980802e-03
2.449233820e-02	7.949079786e-03	8.451897237e-03
2.450073697e-02	7.923155166e-03	7.868485049e-03
2.451167824e-02	7.889241397e-03	7.286198486e-03
2.454235165e-02	7.793296844e-03	6.125580671e-03
2.462858834e-02	7.516324648e-03	4.185694498e-03
2.472737388e-02	7.184669854e-03	2.830314918e-03
2.481308947e-02	6.882811272e-03	1.998872571e-03
2.486849777e-02	6.679844205e-03	1.570657405e-03
2.493196102e-02	6.438930026e-03	1.160374987e-03
2.498214411e-02	6.241392137e-03	8.870072628e-04
2.503814609e-02	6.012798053e-03	6.278573335e-04
2.506784043e-02	5.887773435e-03	5.082574441e-04
2.509873417e-02	5.754654027e-03	3.961674229e-04
2.512658748e-02	5.631793828e-03	3.055450050e-04
2.518324825e-02	5.372756063e-03	1.502381580e-04
2.524106726e-02	5.094214720e-03	3.061962762e-05
2.527155349e-02	4.940757435e-03	-1.686374438e-05

2.532699075e-02	4.648229720e-03	-7.467085075e-05
2.538013694e-02	4.348695069e-03	-9.270253288e-05
2.542149356e-02	4.100020145e-03	-7.847979333e-05
2.547093949e-02	3.780706453e-03	-2.409297106e-05
2.551552164e-02	3.467081719e-03	6.603747873e-05
2.555316099e-02	3.177807978e-03	1.791790300e-04
2.559578611e-02	2.813935564e-03	3.596597861e-04
2.563178577e-02	2.464560466e-03	5.704793621e-04
2.566444604e-02	2.097310025e-03	8.292288708e-04
2.569048182e-02	1.749755344e-03	1.107239592e-03
2.571536841e-02	1.335038455e-03	1.478966181e-03
2.573280821e-02	9.407877803e-04	1.870726989e-03
2.574436307e-02	5.387671300e-04	2.307084468e-03
2.574954459e-02	1.531454975e-04	2.759508930e-03
2.574888448e-02	-2.396831115e-04	3.253620425e-03
2.574256766e-02	-6.186357797e-04	3.761336074e-03
2.572096080e-02	-1.222569290e-03	4.632251740e-03
2.568760725e-02	-1.791461315e-03	5.521663303e-03
2.559066006e-02	-2.860177917e-03	7.374109170e-03
2.545624688e-02	-3.878401093e-03	9.366670985e-03
2.537572281e-02	-4.374379017e-03	1.042219273e-02
2.533317721e-02	-4.614394032e-03	1.095418532e-02
2.528924370e-02	-4.849397201e-03	1.148884045e-02
2.525265725e-02	-5.036447322e-03	1.192431247e-02
2.518793505e-02	-5.350740875e-03	1.267659848e-02
2.512128129e-02	-5.655415677e-03	1.343166732e-02
2.498302858e-02	-6.237850838e-03	1.494963467e-02
2.483511724e-02	-6.802900247e-03	1.652371201e-02
2.468327637e-02	-7.334737064e-03	1.810765434e-02
2.452490374e-02	-7.848031386e-03	1.974262329e-02
2.436530435e-02	-8.330332772e-03	2.138702605e-02
2.420213638e-02	-8.793127685e-03	2.307864633e-02
2.404036082e-02	-9.226242554e-03	2.477954079e-02
2.387802564e-02	-9.638588671e-03	2.652419997e-02
2.371967239e-02	-1.002195798e-02	2.827815877e-02
2.356980430e-02	-1.036951422e-02	3.000045754e-02
2.339709813e-02	-1.075352496e-02	3.208603422e-02
2.323507222e-02	-1.109927561e-02	3.417721630e-02
2.294645795e-02	-1.168428720e-02	3.840296367e-02
2.271461563e-02	-1.212883905e-02	4.267385134e-02
2.254805758e-02	-1.243573880e-02	4.698591026e-02
2.249065748e-02	-1.253925142e-02	4.918345124e-02
2.243219965e-02	-1.264353268e-02	5.363885084e-02
2.245118171e-02	-1.260979539e-02	5.811317639e-02
2.254267057e-02	-1.244550133e-02	6.262391223e-02
2.268370758e-02	-1.218654628e-02	6.723934260e-02
2.286887620e-02	-1.183541303e-02	7.197416824e-02
2.310366657e-02	-1.137027226e-02	7.701426957e-02
2.345053200e-02	-1.063649607e-02	8.351120034e-02
2.383412994e-02	-9.746627625e-03	9.007578857e-02
2.423542181e-02	-8.700967174e-03	9.670332142e-02

2.445361636e-02	-8.067412656e-03	1.003298450e-01
2.485855918e-02	-6.716735473e-03	1.073589189e-01
2.521432913e-02	-5.224950365e-03	1.143010615e-01
2.549584085e-02	-3.608960958e-03	1.211103436e-01
2.570162110e-02	-1.577711306e-03	1.303597072e-01
2.574395931e-02	-5.577268378e-04	1.350042408e-01
2.574584929e-02	4.623247072e-04	1.396490799e-01
2.572924234e-02	1.033725581e-03	1.422509730e-01
2.571617378e-02	1.319433920e-03	1.435519555e-01
2.569992221e-02	1.605147537e-03	1.448529621e-01
2.568950344e-02	1.764061442e-03	1.455765819e-01
2.567473835e-02	1.967310470e-03	1.462888724e-01
2.564065928e-02	2.370462287e-03	1.471870655e-01
2.558196113e-02	2.936965200e-03	1.480347370e-01
# Profile 1 at 99.5000%		
1.742126181e-01	3.609181674e-03	1.487477016e-01
1.742034621e-01	4.026944104e-03	1.491238565e-01
1.741982104e-01	4.248055702e-03	1.493229463e-01
1.741933041e-01	4.444693743e-03	1.495000000e-01
1.741863527e-01	4.709250358e-03	1.495000000e-01
1.741789995e-01	4.973796110e-03	1.495000000e-01
1.741793944e-01	4.959945523e-03	1.492357151e-01
1.741798503e-01	4.943910410e-03	1.489297469e-01
1.741803047e-01	4.927875297e-03	1.486237787e-01
1.741812091e-01	4.895805071e-03	1.480118423e-01
1.741830001e-01	4.831664617e-03	1.467879695e-01
1.741865112e-01	4.703383703e-03	1.443402239e-01
1.741901095e-01	4.568177487e-03	1.417603356e-01
1.741936028e-01	4.432971259e-03	1.391804471e-01
1.742005532e-01	4.150875250e-03	1.325175081e-01
1.742085830e-01	3.798961440e-03	1.212234235e-01
1.742119444e-01	3.641557048e-03	1.125834169e-01
1.742131598e-01	3.582937811e-03	1.014744483e-01
1.742125415e-01	3.612876137e-03	9.588757864e-02
1.742111305e-01	3.680286737e-03	9.030056507e-02
1.742092115e-01	3.770028809e-03	8.532759261e-02
1.742058897e-01	3.920523898e-03	7.901282563e-02
1.742016104e-01	4.106269084e-03	7.269908626e-02
1.741960720e-01	4.334859036e-03	6.596572540e-02
1.741896572e-01	4.585393652e-03	5.923300447e-02
1.741836750e-01	4.807273499e-03	5.457356675e-02
1.741696574e-01	5.290835963e-03	4.698629928e-02
1.741492858e-01	5.923576600e-03	3.905641788e-02
1.741221463e-01	6.673878679e-03	3.065036915e-02
1.740898429e-01	7.469210643e-03	2.141845788e-02
1.740728554e-01	7.855159280e-03	1.548465120e-02
1.740674603e-01	7.973818184e-03	1.209347839e-02
1.740668344e-01	7.987468332e-03	1.040169512e-02
1.740681734e-01	7.958234295e-03	8.711071678e-03
1.740707166e-01	7.902411799e-03	7.495508949e-03

1.740749490e-01	7.808625217e-03	6.280972927e-03
1.740797087e-01	7.701786697e-03	5.339035480e-03
1.740826769e-01	7.634402057e-03	4.868444400e-03
1.740843285e-01	7.596649706e-03	4.633258644e-03
1.740861009e-01	7.555923439e-03	4.398153301e-03
1.740878109e-01	7.516421779e-03	4.186197875e-03
1.740908444e-01	7.445829867e-03	3.840806502e-03
1.740941901e-01	7.367188702e-03	3.497826972e-03
1.741019446e-01	7.181600289e-03	2.820348995e-03
1.741097619e-01	6.989513395e-03	2.261961814e-03
1.741190673e-01	6.753732489e-03	1.716664374e-03
1.741264417e-01	6.560853118e-03	1.356287147e-03
1.741347090e-01	6.337636417e-03	1.013891854e-03
1.741411427e-01	6.158321439e-03	7.863212719e-04
1.741491902e-01	5.926384796e-03	5.436543728e-04
1.741534473e-01	5.799938672e-03	4.326146882e-04
1.741578692e-01	5.665606542e-03	3.293221302e-04
1.741619261e-01	5.539495224e-03	2.449041126e-04
1.741701351e-01	5.275088290e-03	1.031053605e-04
1.741784587e-01	4.992695851e-03	-2.177513141e-06
1.741826344e-01	4.844830778e-03	-4.039692669e-05
1.741906133e-01	4.548925528e-03	-8.509697385e-05
1.741982041e-01	4.248317595e-03	-9.004503027e-05
1.742075357e-01	3.846686747e-03	-3.851325799e-05
1.742143951e-01	3.522361855e-03	4.762517183e-05
1.742205008e-01	3.206180951e-03	1.668645638e-04
1.742236118e-01	3.032424302e-03	2.463257162e-04
1.742268858e-01	2.838092726e-03	3.464131492e-04
1.742298695e-01	2.648598649e-03	4.549822462e-04
1.742350532e-01	2.282268304e-03	6.943142474e-04
1.742411832e-01	1.752880048e-03	1.104601741e-03
1.742476392e-01	9.070389933e-04	1.905949827e-03
1.742499783e-01	8.705302434e-05	2.840312574e-03
1.742485372e-01	-7.139928421e-04	3.893834032e-03
1.742435452e-01	-1.499820759e-03	5.057334461e-03
1.742368413e-01	-2.141412891e-03	6.102062831e-03
1.742186312e-01	-3.306215379e-03	8.218837386e-03
1.741943325e-01	-4.404204001e-03	1.048753470e-02
1.741650716e-01	-5.439700582e-03	1.289438353e-02
1.741487850e-01	-5.938281897e-03	1.415636735e-02
1.741319116e-01	-6.414036948e-03	1.542916005e-02
1.741152601e-01	-6.851182309e-03	1.666323797e-02
1.740916476e-01	-7.427026518e-03	1.839352581e-02
1.740678668e-01	-7.964937988e-03	2.013105938e-02
1.740196812e-01	-8.956173916e-03	2.370460709e-02
1.739726170e-01	-9.828072932e-03	2.737373860e-02
1.739283493e-01	-1.058261903e-02	3.113097344e-02
1.738883681e-01	-1.122042573e-02	3.497003202e-02
1.738539407e-01	-1.174179732e-02	3.888578652e-02
1.738261581e-01	-1.214616296e-02	4.287378790e-02
1.738150169e-01	-1.230456894e-02	4.489906252e-02

1.738102021e-01	-1.237239489e-02	4.591388136e-02
1.738059021e-01	-1.243265390e-02	4.693015127e-02
1.738031963e-01	-1.247042390e-02	4.764408135e-02
1.737992779e-01	-1.252491513e-02	4.882900199e-02
1.737960717e-01	-1.256932689e-02	5.001368262e-02
1.737917975e-01	-1.262828645e-02	5.238233270e-02
1.737917765e-01	-1.262857497e-02	5.714914504e-02
1.738027826e-01	-1.247618830e-02	6.195067031e-02
1.738216388e-01	-1.221066647e-02	6.686459138e-02
1.738472291e-01	-1.184075244e-02	7.190976860e-02
1.738753689e-01	-1.142009645e-02	7.651890340e-02
1.739227391e-01	-1.067442463e-02	8.320488448e-02
1.739759642e-01	-9.768642489e-03	8.992541739e-02
1.740040056e-01	-9.255729410e-03	9.330292409e-02
1.740323953e-01	-8.705623925e-03	9.667572000e-02
1.740597417e-01	-8.140565286e-03	9.992335933e-02
1.740891598e-01	-7.485114193e-03	1.034639685e-01
1.741176434e-01	-6.790342089e-03	1.069963828e-01
1.741700077e-01	-5.279291628e-03	1.140604045e-01
1.742126227e-01	-3.608960958e-03	1.211103436e-01
1.742352693e-01	-2.265709142e-03	1.272268859e-01
1.742475583e-01	-9.224548032e-04	1.333434398e-01
1.742496605e-01	3.439776911e-04	1.391101827e-01
1.742472599e-01	9.771947790e-04	1.419935581e-01
1.742451967e-01	1.293803533e-03	1.434352467e-01
1.742439493e-01	1.452107963e-03	1.441560912e-01
1.742425582e-01	1.610412428e-03	1.448769359e-01
1.742410703e-01	1.764061442e-03	1.455765819e-01
1.742389853e-01	1.959209086e-03	1.462658016e-01
1.742340160e-01	2.360118445e-03	1.471682325e-01
1.742253456e-01	2.931116111e-03	1.480274061e-01

